RESEARCH

A deep phenotyping study in mouse and iPSC models to understand the role of oligodendroglia in optic neuropathy in Wolfram syndrome

K. Ahuja[1,2,3†], M. Vandenabeele[1,2†], F. Nami[3†], E. Lefevere[1], J. Van hoecke[1], S. Bergmans[2], M. Claes[1], T. Vervliet[4], K. Neyrinck[3], T. Burg[5,6], D. De Herdt[1], P. Bhaskar[3], Y. Zhu[3], Z. J. Looser[7], J. Loncke[4], W. Gsell[8], M. Plaas[9], P. Agostinis[10], J. V. Swinnen[11], L. Van Den Bosch[5,6], G. Bultynck[4], A. S. Saab[7], E. Wolfs[12], Y. C. Chai[3], U. Himmelreich[8], C. Verfaillie[3], L. Moons[2] and L. De Groef[1*]

Abstract

Wolfram syndrome (WS) is a rare childhood disease characterized by diabetes mellitus, diabetes insipidus, blindness, deafness, neurodegeneration and eventually early death, due to autosomal recessive mutations in the *WFS1* (and *WFS2*) gene. While it is categorized as a neurodegenerative disease, it is increasingly becoming clear that other cell types besides neurons may be affected and contribute to the pathogenesis. MRI studies in patients and phenotyping studies in WS rodent models indicate white matter/myelin loss, implicating a role for oligodendroglia in WS-associated neurodegeneration. In this study, we sought to determine if oligodendroglia are affected in WS and whether their dysfunction may be the primary cause of the observed optic neuropathy and brain neurodegeneration. We demonstrate that 7.5-month-old $Wfs1^{\Delta exon8}$ mice display signs of abnormal myelination and a reduced number of oligodendrocyte precursor cells (OPCs) as well as abnormal axonal conduction in the optic nerve. An MRI study of the brain furthermore revealed grey and white matter loss in the cerebellum, brainstem, and superior colliculus, as is seen in WS patients. To further dissect the role of oligodendroglia in WS, we performed a transcriptomics study of WS patient iPSC-derived OPCs and pre-myelinating oligodendrocytes. Transcriptional changes compared to isogenic control cells were found for genes with a role in ER function. However, a deep phenotyping study of these WS patient iPSC-derived oligodendroglia unveiled normal differentiation, mitochondria-associated endoplasmic reticulum (ER) membrane interactions and mitochondrial function, and no overt signs of ER stress. Overall, the current study indicates that oligodendroglia functions are largely preserved in the WS mouse and patient iPSC-derived models used in this study. These findings do not support a major defect in oligodendroglia function as the primary cause of WS, and warrant further investigation of neurons and neuron-oligodendroglia interactions as a target for future neuroprotective or -restorative treatments for WS.

†Ahuja K., Vandenabeele M. and Nami F. are Joint first authors.

*Correspondence:
L. De Groef
lies.degroef@kuleuven.be

Full list of author information is available at the end of the article

Introduction

Wolfram syndrome (WS) type 1 is a rare hereditary disease caused in most cases by recessive mutations in the Wolfram syndrome 1 (*WFS1)* gene [24, 77]. The disease symptoms are often referred to as 'DIDMOAD', an acronym of diabetes insipidus, diabetes mellitus, optic atrophy and deafness. However, patients may also experience a range of other (neurological) symptoms, including ataxia, urinary tract problems, psychiatric problems, apnea and autonomic dysfunction [13, 32]. The disease manifests in early childhood and gradually worsens until patients die around the age of 30 years, mostly due to respiratory failure caused by brainstem atrophy [77]. *WFS1* is located on chromosome 4p16 and consists of 8 exons, spanning 33.4 kilobase pairs of the human genome. The WS prevalence is 1 in 770.000 globally, 1 in 100.000 in North America and the highest prevalence is 1 in 68.000 in Lebanon. However, heterozygous carrier frequency reaches as high as 1 in 100 in Europe and the US [7, 64] and has been linked to hearing loss and psychiatric diseases [25]. Studies have revealed more than 170 distinct mutations in *WFS1*, which are mostly inactivating (nonsense and frameshift) and the majority are located in exon 8, albeit mutations were also found in other parts of the gene [64]. WFS1 is highly expressed in different organs, including pancreas, brain (cerebellum, enthorinal cortex, olfactory bulb and hippocampus), retina, inner ear, kidney, heart, endocrine tissues, testis, fallopian tubes, and placenta [9, 12, 60, 70, 74]. Given the monogenic cause of the disease, research efforts have focused on elucidating the role of the WFS1 protein in WS pathogenesis. In Wolfram patients, loss-of-function and missense mutations lead to a complete absence or a decreased stability of the WFS1 protein, suggesting that WS is caused by a loss of WFS1 function [20, 24].

Wolframin, the protein encoded by the *WFS1* gene, is an endoplasmic reticulum (ER) membrane protein that regulates the ER stress response [16] and cellular Ca^{2+} concentrations [75, 82]. It is proposed that WFS1 deficiency partakes in the unfolded protein response pathway triggered by ER stress, which, if unresolved, initiates apoptotic pathways leading to neuronal and pancreatic beta cell loss. More recently, a crucial role for WFS1 at the mitochondria-associated ER membranes (MAMs) has been identified [13, 37]. By regulating MAM function and integrity, WFS1 is a key regulator of ER-mitochondria cross-talk, and thereby affects Ca^{2+} transfer and lipid signaling between ER and mitochondria [3, 75, 82], and mitochondrial biogenesis and dynamics [9, 26, 83]. As such, WFS1 deficiency leads to mitochondrial dysfunction and mitophagy, with a detrimental effect on viability and bioenergetics of WS neurons.

Notably, until today, research has mainly focused on the diabetic phenotype of WS and the aforementioned WFS1 functions have mostly been studied in the islets of Langerhans and b-cells of the pancreas [18, 28]. However, diabetes has become a chronic illness that can be managed via drug therapy and only has a limited impact on the quality of life of Wolfram patients. This contrasts with the neurodegenerative phenotype of the disease, which is devastating and cannot be controlled by any means. In recent years, efforts to improve our knowledge on the neuronal phenotype of Wolfram patients and *Wfs1* animal models ensued. In neurons, WFS1 deficiency has been associated with MAM dysregulation, impaired neurite outgrowth and synapse formation, and increased cytosolic Ca^{2+} concentration [59, 83]. A recent study using brain organoids showed that this abnormal synapse formation and function goes hand in hand with decreased expression of the excitatory amino acid transporter 2 (EAAT2) and compromised glutamate clearance in astrocytes [81]. MRI studies in Wolfram patients found white matter changes and volume loss in different brain regions, most prominently in the brainstem, cerebellum and optic radiations, already early in the disease pathogenesis [19, 42]. In addition, optic nerve and brainstem degeneration, as well as optic nerve demyelination, have also been observed in *Wfs1* rat and mouse models [9, 58]. In the *Wfs1*$^{\Delta exon8}$ mouse model, disturbances in the dopaminergic and GABAergic system, together with changes in motor function and anxiety have been described, thereby mirroring the motor and psychiatric problems seen in patients [44, 62, 79]. Furthermore, a recent study by Rossi et al. reported that retinal degeneration and vision loss in the *Wfs1*$^{\Delta exon8}$ mouse model is preceded by loss of glial homeostasis, MCT1-dependent metabolic dysfunction and myelin derangement in the optic nerve [66]. While these studies all find a clear neurodegenerative phenotype, they also show white matter defects, hence raising the question whether the neurodegenerative component of WS could be mainly driven by an oligodendroglia rather than a neuronal pathology. Oligodendrocytes, due to their continuous, high production of myelin, are particularly sensitive to ER stress [35], and their dysfunction or loss will have detrimental consequences for the highly energy-demanding neurons. In that case, neurodegeneration in WS might relate to the loss of the supportive functions that are being fulfilled by oligodendroglia in the central nervous system (CNS). Indeed, oligodendrocytes physically protect and increase conductivity by insulating axons with myelin sheaths,

but oligodendroglia also provide metabolic support to axons by transferring metabolites, like lactate or pyruvate, to fuel the axonal energy production [52, 67], and they support the formation and function of neuronal synapses and neural circuits [50, 76]. Thus, dysfunction or loss of oligodendroglia might substantially contribute to neurodegeneration.

In this study, we combined a neuropathological analysis of the retina, optic nerve and brain of a WS mouse model with a deep phenotyping study of WS patient iPSC-derived oligodendroglia, to disentangle the role of the oligodendroglia in WS pathogenesis. Our investigations reveal that the *Wfs1* KO mouse presents with grey and white matter abnormalities in the brain, and abnormal axonal conduction combined with subtle thinning of the myelin sheath and a reduction of the oligodendrocyte precursor (OPC) pool in the optic nerve. Next, a differential transcriptomics study of oligodendroglia (i.e., OPCs and premyelinating oligodendrocytes) derived from WS patient versus isogenic control iPSCs led to the identification of several genes that have previously been linked with WS-like syndromes characterized by impaired vision and hearing, as well as cellular processes previously linked to WFS1 deficiency, such as ER function. However, in vitro assays using WS patient iPSC-derived oligodendroglia did not uncover any signs of ER stress, abnormal ER-mitochondria interactions, or mitochondrial dysfunction. Hence, we conclude that cell-intrinsic defects in oligodendroglia are minor and unlikely to be the primary cause of WS, and that future research should focus on the neurons and their intricate interactions with oligodendroglia that govern CNS function and integrity.

Materials and methods
Experimental animals
All experiments were performed using $Wfs1^{\Delta exon8}$ mice (*Wfs1* KO mice) and wild type littermates (129S6/SvEvTac and C57BL/6 mixed background). This mouse model was originally created by Luuk et al. and has a disrupted exon 8 in the *Wfs1* gene [44]. Mice were bred under standard laboratory conditions and had free access to food and water. Mice of both sexes were used, at the age of 3 months (±1 week), 4.5 months (±1 week), 6 months (±2 weeks) or 7.5 months (±2 weeks). Occasionally, animals had an opaque cornea. These were excluded from the study.

Optical coherence tomography
Upon general anesthesia (75 mg/kg ketamine and 1 mg/kg medetomidine) and pupil dilatation (0.5% tropicamide), optical coherence tomography scans of the retina (1000 A-scans, 100 B-scans, 1.4×1.4 mm) (Envisu R2200, Bioptigen) were acquired. Anesthesia was reversed with atipamezole (1 mg/kg). Retinal layer

thickness was measured using InVivoVue Diver 3.0.8 software (Bioptigen), at 16 locations equally spaced around the optic nerve head and averaged per mouse, all as described in [78].

Optomotor response test
Visual performance was tested using the virtual reality optomotor test (Optomotry, Cerebral Mechanics), as previously described [72, 78]. Briefly, the unrestrained mouse was placed on a platform in the testing arena and vertical black-white sine-wave gratings were projected on the screens. A video camera was placed on top of the arena to provide real-time video data. Spatial frequency thresholds were measured for each eye under 100% contrast, via a simple staircase procedure. The highest spatial frequency that the mouse could track was identified as the visual acuity. For contrast sensitivity, a similar approach was used, but contrast was systematically reduced until the contrast threshold was identified. Contrast threshold was identified at three spatial frequencies (0.103, 0.192, 0.272 cyc/deg), and calculated as described in [61].

Electroretinograms and visual evoked potentials
Following overnight dark adaptation, electroretinograms (Celeris, Diagnosys) were recorded for anesthetized mice (75 mg/kg ketamine and 1 mg/kg medetomidine) as described in [11]. Lens electrodes with integrated stimulators were placed on the cornea after pupil dilation (0.5% tropicamide and 15% phenylephrine), and a needle scalp electrode was inserted above the midline near the visual cortex. The ground and reference electrode were placed in the tail base and cheek, respectively. Eyes were alternately stimulated, and full field visual evoked potential responses were recorded at a single flash intensity of 0.05 cd*s/m^2, averaging 300 brief flashes with an inter-sweep delay of 690 ms. To measure the scotopic threshold response, the responses from 50 light flashes with a single-flash intensity of 0.0001 cd·s/m^2 and an inter-sweep delay of 1 s were averaged. Anesthesia was reversed with atipamezole (1 mg/kg). Data were analyzed with Espion v6.65.1 software (Diagnosys) according to [11]. Visual evoked potential and scotopic threshold response amplitudes were defined as the amplitude from the baseline to the trough of the negative visual evoked potential response, and from the baseline to the peak of the positive scotopic threshold response, respectively.

Ex vivo compound action potentials
Acute optic nerve preparations for compound action potential (CAP) recordings were carried out as previously described [38]. In brief, optic nerves were isolated after isoflurane anesthesia and decapitation and placed in an interface perfusion chamber (Haas Top, Harvard

Apparatus), perfused with artificial cerebrospinal fluid (ACSF containing in mM: 126 NaCl, 3 KCl, 2 $CaCl_2$, 1.25 NaH_2PO_4, 26 $NaHCO_3$, 2 $MgSO_4$, 10 glucose, pH 7.4) at 37 °C using a TC-10 temperature control system (npi electronic), and continuously oxygenated with 95% O_2 and 5% CO_2. Nerve ends were inserted into custom-made suction electrodes filled with ACSF and stimulated evoking the CAP. The optic nerve was first stimulated at 0.4 Hz for 1 min to obtain baseline values, followed by a stepwise increase in stimulation frequency, with intervals of 1 min at frequencies of 1, 10, 25, and 50 Hz and a recovery period of 10 min with 0.4 Hz.

Magnetic resonance imaging

Mice were anaesthetized with isofluorane (2.5% induction, 1-1.5% for maintenance). Body temperature was kept constant at 37 ± 1 °C, respiration rate was monitored during scanning and kept above 80 min^{-1} by adjusting isoflurane concentrations. MR images were acquired using a 9.4 Tesla preclinical MR scanner with a horizontal bore of 20 cm (Biospec 94/20, Bruker Biospin) and equipped with an actively shielded gradient set of up to 600 mT m^{-1}. Brain images were acquired using a linearly polarized resonator (transmit) in combination with an actively decoupled surface coil for the mouse brain (Bruker Biospin) as previously described [71]. For the acquisition of manganese enhance MRI, mice received a unilateral intravitreal injection of 2 µl of 0.5 M $MnCl_2$ 20 to 24 h before image acquisition, similar to previous reports [36].

MRI was performed at the age of 3, 4.5, 6 and 7.5 months. After initial localizer images, T_2-weighted two-dimensional (2D) MRI scans of the brain were acquired in axial orientation using a spin-echo sequence (rapid acquisition with relaxation enhancement, RARE). Acquisition parameters: repetition time (TR)=2500ms, echo time (TE)=33ms, RARE factor (RF)=8, 20 slices, 0.7 mm slice thickness, 70 µm in plane resolution and number of averages (NA)=1. For the analysis of Mn^{2+} distribution T_1-weighted MRI were acquired using a 3D gradient echo sequence (FLASH) with TR=30 ms, TE=5 ms, 60º pulse, NA=2, field of view (FOV)=2.0×1.5×1.5 cm and an isotropic spatial resolution of 156 µm. T_1 maps were determined using a spin echo multiple TR sequence (RAREVTR) with TE=20 ms, RF=8, NA=2, TR=500, 750, 1500, 2500, 6000 ms and geometric parameters as for the 2D with an in-plane resolution of 125 µm. Finally, diffusion MRI was acquired for the calculation of apparent diffusion coefficients (ADC), mean diffusivity (MD) and fractional anisotropy (FA). Parameters for diffusion MRI were as following: TR=750 ms, TE=20 ms, NA=1, spin echo readout, 6 directions, b-values=0, 100, 600, 1200 s/mm^3, and geometric parameters as for the 2D with an in-plane resolution of 125 µm. The Bruker software ParaVision was used for image acquisition, processing and calculation of parametric maps. Examples for the respective images are shown in supplementary figure S1.

Human induced pluripotent stem cell culture

Two WS patient derived induced pluripotent stem cell (iPSC) lines (kindly provided by Prof. F. Urano, Washington University School of Medicine), and their genetically corrected isogenic controls made by adenosine base editing [51], have been used in this study: patient 1, with a homozygous point mutation at c.2002 C>T [p.Q668X], and patient 2, with compound heterozygous mutations at c.376G>A [p.A126T] and c.1838G>A [p.W613X]. Phenotypic characteristics of these patients have previously been described in [45].

Both patient and isogenic iPSC lines were cultured as described in [85], on human Matrigel (VWR)-coated 6-well plates (Corning) in E8 basal medium (Gibco) complemented with E8 supplement Flex (Gibco) and 5 U/ml Penicillin-Streptomycin (Gibco), and passaged two times a week using 0.5 mM EDTA (Gibco) (in PBS). Routine checkups for mycoplasma contamination were done using MycoAlert Mycoplasma Detection Kit (Lonza) to ensure data reliability.

Differentiation of iPSCs to OPCs and pre-myelinating oligodendrocytes

All iPSC lines were differentiated to OPCs and pre-myelinating oligodendrocytes (OPCs/pmOLs), using overexpression of the transcription factor *SOX10*, as described in Garcia-Leon et al. [17]. *SOX10* overexpression iPSCs were dissociated with accutase (Sigma) and plated at 25,000 cells/cm^2 in a 6-well plate. Oligodendrocyte induction was done by adding neurobasal medium supplemented with 0.1 µM RA (Sigma), 10µM SB431542 (Tocris), and 1µM LDN-193,189 (Milteny) for the next 6 days. From day 7 on, medium was replaced with neurobasal medium containing 0.1 µM RA, and 1µM SAG (Milllipore) for 3 days. The cells were then dissociated with accutase (Sigma) and replated at 50,000–75,000 cells/cm^2 in a poly-L-ornithin-laminin coated 6-well plate with neurobasal medium supplemented with 10 ng/ml PDGFaa (Peprotech), 10 ng/ml IGF1 (Peprotech), 5ng/ml HGF (Peprotech), 10 ng/ml NT3 (Peprotech), 60 ng/ml T3 (Sigma), 100 ng/ml Biotin (Sigma), 1 µM cAMP (Sigma), and 5 µg/ml doxycycline (Sigma) (from here on referred to as oligodendrocyte maturation medium (OMM)) to induce oligodendrocyte fate, until day 23. On day 24, the cells were dissociated with accutase, characterized for pmOL expression markers (O4 and MBP) by either fluorescence-activated cell sorting (data not shown) and/or immunofluorescence, and used for experiments or cryopreserved in liquid nitrogen for future use.

RT-qPCR

Total RNA was isolated and purified using the Quick-RNA Microprep Kit (Zymo research), and cDNA preparation was done with the SuperScript™ III First-Strand Synthesis System kit (Thermofisher), on 500ng-1ug RNA, according to the manufacturer's instructions. RT-qPCR for oligodendrocyte lineage markers was performed using Platinum SYBR Green qPCR Supermix-UDG (Thermofisher). The sequence of the primers is listed in supplementary table S1.

X-box-binding protein 1 (XBP1) splicing assay

RNA isolation was performed as described above, with the Quick-RNA Microprep Kit (Zymo research) and SuperScript™ III First-Strand Synthesis System kit (Thermofisher). Next, 140 ng cDNA was used to set-up a PCR reaction using Platinum® Taq mix (Invitrogen™) (Supplementary Table 1). The PCR product was run on 2.5% agarose/1x TAE gel with SYBR Safe. In addition to the spliced and unspliced amplicon, a hybrid amplicon was also seen in the gel. Quantification was done as the ratio of spliced amplicon (spliced amplicon+50% of the hybrid amplicon) and total XBP1 amplicon (spliced+unspliced+hybrid amplicon) using ImageJ [65].

Real time cell metabolic analysis

OPCs/pmOLs were plated on a Seahorse XF24 (Agilent) Extracellular Flux Analyzer culture plate in OMM supplemented with 5 µg/ml doxycycline (Sigma) and RevitaCell supplement (Gibco). The next day, medium change with Mito Stress assay medium (Agilent) containing 10 mM glucose, 2 mM glutamine and 1 mM sodium pyruvate was done one hour before the Mito Stress assay. Addition of 1 µM oligomycin (Sigma-Aldrich), 2.0 µM FCCP (Sanbio) and 0.5 µM antimycin A (Sigma-Aldrich), allowed to detect the mitochondrial respiration activity. After the assay, cells were detached using accutase and counted with an automated cell counter (Nucleocounter 900-002, Chemometec) to enable normalization.

Intracellular Ca^{2+} measurements

OPCs/pmOLs were plated on a 4-chambered glass bottom dish (Cellvis) in OMM supplemented with 5 µg/ml doxycycline (Sigma) and RevitaCell (Gibco). After 2 days, Ca^{2+} recording was performed by loading 1.25 µM Cal-520AM (Abcam, ab171868) in OMM for one hour. PBS washing was performed twice, followed by addition of modified Krebs-Ringer solution (135 mM NaCl, 6.2 mM KCl, 1.2 mM MgCl$_2$, 12 mM HEPES, pH 7.3, 11.5 mM glucose and 2 mM CaCl$_2$) for imaging. For imaging (eclipse Ti2, Nikon), a baseline was recorded for 30 s followed by addition of different stimulants (10 µM ATP or 10 µM acetylcholine). Cal-520 was excited at 480 nm, after which fluorescent intensity alterations were measured at 510 nm. Area under the curve and peak intensity were quantified using ImageJ software. Fluorescent signals were plotted as F/F_0, with F_0 the mean Cal-520AM fluorescent intensity from the first 10 s of the baseline measurement [53].

Proximity ligation assay

The proximity ligation assay was done as described in [85] and based on the manufacturer's protocol, using the Duolink® Proximity Ligation Assay kit (Sigma-Aldrich). Briefly, OPCs/pmOLs were plated on a 16 well CultureWell™ Chambered Coverglass (Invitrogen) in OMM supplemented with 5 µg/ml doxycycline (Sigma) and RevitaCell (Gibco). After 2 days, the cells were fixed with 4% paraformaldehyde (PFA) (Thermo Fisher) for 10 min, permeabilized with 0.1% Triton X100 in PBS and incubated overnight with the primary antibodies diluted in blocking serum (anti-protein tyrosine phosphatase interacting protein 51 (PTPIP51) (Abcam, ab224081) and anti-vesicle-associated membrane protein B (VAPB) (RnD Systems, MAB58551)) at 4 °C. Secondary antibodies were added to the cells in blocking serum for 1 h at 37 °C. Further ligation and amplification were performed by adding ligation buffer for 90 min, and amplification buffer for 100 min, at 37 °C. Lastly, slides were mounted with Duolink In Situ Mounting Medium containing 4′,6-diamidino-2-phenylindole (DAPI). Primary antibodies were omitted as a negative control. Quantification of VAPB-PTPIP51 interactions was done on confocal microscopy images (C2, Nikon), using ImageJ software, as described [40].

Lipidomics

Lipids were extracted from a pellet of 500,000 cells, homogenized in 700 µl water with a handheld sonicator, and mixed with 800 µl 1 N HCl: CH$_3$OH 1:8 (v/v), 900 µl CHCl$_3$ and 200 µg/ml 2,6-di-tert-butyl-4-methylphenol (BHT; Sigma-Aldrich), 3 µl of SPLASH® LIPIDOMIX® Mass Spec Standard (Avanti Polar Lipids, 330707), and 3 µl of Ceramides and 3 µl of Hexosylceramides Internal Standards (cat. no. 5040167 and 5040398, AB SCIEX). The organic phase was rated and evaporated by Savant Speedvac spd111v (Thermo Fisher Scientific) at RT for 1–2 h. The remaining lipid pellets were stored in -80 °C for further use.

Lipid pellets were reconstituted in 100% ethanol and ran on liquid chromatography electrospray ionization tandem mass spectrometry to identify several lipid classes. Sphingomyelin, cholesterol esters, ceramides, hexose-ceramides, and lactose-ceramides were measured in positive ion mode with a precursor scan of 184.1, 369.4, 264.4, 266.4, 264.4, and 264.4, respectively. Triglycerides, diglycerides and monoglycerides were measured in positive ion mode with a neutral loss scan

for one of the fatty acyl moieties. Phosphatidylcholine, alkylphosphatidylcholine, alkenylphosphatidylcholine, lysophosphatidylcholine, phosphatidylethanolamine, alkylphosphatidylethanolamine, alkenylphosphatidylethanolamine, lyso phosphatidylethanolamine, phosphatidylglycerol, phosphatidylinositol, and phosphatidylserine were measured in negative ion mode by fatty acyl fragment ions. Lipid quantification was performed by scheduled multiple reactions monitoring, the transitions being based on the neutral losses or the typical product ions as described above.

Peak integration was performed with the Multi-QuantTM software version 3.0.3. Lipid species signals were corrected for isotopic contributions (calculated with Python Molmass 2019.1.1). The total lipid amount and concentration per lipid class were determined with absolute values in nmol/mg DNA. The lipidomic dataset was analysed with the web-based application Metabo-Analyst 5.0 [55]. Missing values were addressed through imputation. Lipid species with >50% missing values were removed, and the remaining missing values were substituted by LoDs (1/5 of the smallest positive value of each variable). To prepare data for univariate and multivariate analyses, data were log10 transformed and Pareto scaling was applied (mean-centred and divided by the square root of the standard deviation of each variable). Groups were compared using principal component analysis and hierarchical clustering heatmaps (distance measure: Euclidean, clustering algorithm: ward, standardization: auto-scale features). This multivariate-based approach identified a technical outliner with very high lipid concentrations compared to all the other samples, which was removed from the analysis.

Transcriptomics
Total RNA was extracted from OPCs/pmOLs using the Quick-RNA Microprep Kit (Zymo research). Libraries were prepared from 500 ng using the QuantSeq 3' mRNA-seq library prep kit (Lexogen), and pooled equimolar to 2 nM for single-read sequencing on the HiSeq4000 (Illumina) with settings 51-8-8. Quality control of the generated raw fastq sequence files was performed with FastQC v0.11.7 [2], and adapters were filtered with ea-utils fastq-mcf v1.05 [4]. Splice-aware alignment was performed with HiSat2 [23] against the human reference genome hg38 using default parameters. Reads mapping to multiple loci in the reference genome were discarded. Resulting BAM alignment files were handled with Samtools v1.5. [34]. Reads per gene were calculated with HT-seq Count v2.7.14 and count-based differential expression analysis was done with R-based Bioconductor package DESeq2 [41]. Principle component analysis was performed with regularized log transformation for clustering, and limma package was used to remove batch

effects. Cut-off values of adjusted p-value<0.05 and $\log_2$ fold change>1 were used for the enhanced volcano plot. Gene set enrichment analysis was performed using ClusterProfiler [80] and STRING v12.0 [73].

Western blot
Mice were euthanized by an intraperitoneal injection of 60 mg/kg sodium pentobarbital followed by transcardial perfusion with saline, after which the brain, retina and optic nerve were dissected and snap-frozen in liquid nitrogen. Samples were homogenized in lysis buffer (150 mM NaCl, 50 mM Tris-HCl, 10 mM $CaCl_2$dihydrate, 1% Triton-X 100, 0.05% BRIJ-35), supplemented with EDTA-free protease inhibitor cocktail (Roche Applied Science). Western blot was performed as previously described [32]. Briefly, samples (30 µg for retina, 20 µg for optic nerve) were separated on a 4–12% Bis-Tris gel and transferred onto a PDVF membrane, followed by 2 h blocking with 15% milk powder (in TBST) and overnight incubation with rabbit anti-BIP (ref. 3183, Cell signaling, 1/1000 for retina, 1/500 for optic nerve) or mouse anti-CHOP (ref. 895, Cell signaling, 1/1000 for retina, 1/500 for optic nerve). Protein bands were visualized using horseradish peroxidase-labeled secondary antibodies and a luminol-based enhanced chemiluminescence kit. At least two Western blot experiments (i.e., two technical repeats) were performed for each of the lysates. Optical density measurements were normalized against a SWIFT Membrane total protein stain (G-Biosciences), and subsequently presented as a percentage relative to the naive condition.

OPCs/pmOLs were lysed by using M-PER buffer (Thermo Scientific™) containing PhosSTOP™ Phosphatase Inhibitor Cocktail (Roche Diagnostics) and complete™ Protease Inhibitor (Roche Diagnostics). Protein concentration was determined by using a Pierce™ BCA Protein Assay kit (Thermo Scientific™) and 20 µg protein was mixed with SDS-containing reducing sample buffer (Thermo Scientific™), followed by denaturation at 95 °C for 10 min and loading on 4–20% ExpressPlus™ PAGE gels (GenScript). The gel was allowed to run at 120 V for 2 h, followed by 0.2 µm nitrocellulose membrane transfer at 25 V, 2.5 A for 7 min using iBlot™ 2 dry Blotting Transfer system (Thermo Fisher). The membrane was blocked in Tris-buffered saline with Tween-20 (TBST) (Sigma-Aldrich) containing 5% skim milk (Sigma-Aldrich) for 1 h, incubated overnight with primary antibody (BiP, cat. 3183 S dilution 1:1000 or WFS-1 cat. PA5-76065 dilution 1:2000) in 3% bovine serum albumin-TBST at 4 °C. The next day, incubation with secondary antibody diluted in TBST was performed for 1 h. SuperSignal™ West Pico PLUS Chemiluminescent Substrate (Thermo Scientific™) was used for chemiluminescence imaging (ImageQuant LAS4000, GE Healthcare). Beta-actin (ref. 8457, Cell

Signaling, 1/1000) or vinculin (ref. V9131, Sigma, 1/1000) were used as a loading control and for normalization of the measured optical densities.

Immunohistochemistry and morphometric analyses

Mice were euthanized by an intraperitoneal injection of 60 mg/kg sodium pentobarbital, followed by transcardial perfusion with saline and 4% PFA. For retinal flatmounts, the eyes were post-fixated in 4% PFA for 1 h at room temperature, retinas were flatmounted and post-fixated for another hour in 4% PFA at room temperature. For cryosections of the optic nerve, the nerves were immersed in 4% PFA for 30 min at room temperature.

For wholemount immunostaining, wholemounts were frozen for 15 min at -80 °C in PBS + 2% Triton-X and incubated overnight at room temperature with primary antibodies for RNA-binding protein with multiple splicing (RBPMS) (ref. 1830-RBPMS, PhosphoSolutions, 1/250) or TH (ref. AB152, Millipore, 1/1000), followed by incubation with corresponding fluorophore-conjugated secondary antibodies. Washes were performed with PBS + 2% Triton-X. Images were made with a DM6 fluorescence microscope (Leica), and analysed using ImageJ software [41]. RBPMS + retinal ganglion cells were counted using a validated automated counting method [26]. Tyrosine hydroxylase + amacrine cell numbers were counted manually [48].

For cryosections of the optic nerve, tissues were cryoprotected in an ascending sucrose series and embedded in optimal cutting temperature medium (Tissue-Tek, Lab Tech) to make 12 μm thick longitudinal sections. Optic nerve cryosections were blocked with 20% pre-immune donkey serum for 45 min, followed by overnight incubation with the primary antibody for platelet-derived growth factor receptor alpha (PDGFRa) (ref. AF1062-SP, R&D systems, 1/200), OLIG2 (ref. 13999-1-AP, Proteintech, 1/400), or CC1 (anti-adenomatous polyposis coli clone CC1, ref. OP80, Calbiochem, 1/200) and a 2-hour incubation with the secondary fluorophore-conjugated antibody. Washes were performed with TBS with 0.1% Tween-20. Nuclei were counterstained with DAPI and sections were mounted with mowiol. Images were taken with an epifluorescence microscope (DM6 B, Leica Microsystems) and 20X objective. Two or three representative sections were chosen for each optic nerve, on which cells in 3 regions of interest (ROI) of 0.08 mm² were manually counted using the cell-counter plugin of ImageJ: one ROI close to the ONH, one ROI in the middle of the optic nerve and one ROI close to the optic chiasm.

For immunocytochemistry of OPCs/pmOLs, 30,000 cells per well were plated in a 96-well plate in OMM. The cells were maintained for 2 days, followed by fixation with 4% PFA for 15 min at room temperature. The cells were washed, blocked and permeabilized with 5% goat serum (Dako) and 0.1% Triton X-100 (Sigma) for 1 h. Overnight incubation with the primary antibody (MBP, ref. ab9348 dilution 1:75 and O4, ref. MAB1326 dilution 1:1000) diluted in 5% goat serum at 4 °C was followed by secondary antibody incubation, diluted in Dako REAL Antibody Diluent (Dako) for 1 h. Hoechst33342 (Sigma, dilution 1/2 000 in Dako REAL Antibody Diluent) was applied for nuclear counterstaining. Fluorescence imaging was performed using the Operetta High Content Imaging System (PerkinElmer) and analysis was done using automated segmenting and counting of objects using Columbus software (PerkinElmer). Briefly, the nuclear staining was segmented and used as a reference to have object count and cytoplasm segregation. The cell population was selected based on the mean fluorescence intensity in both cell regions (nuclear and cytoplasmic), using a threshold to select the positive population. The integrated fluorescence intensity was measured by dividing the mean fluorescence intensity by the cytoplasm area (in μm²).

Transmission electron microscopy and morphometric analyses

Mice were euthanized by an intraperitoneal injection of 60 mg/kg sodium pentobarbital (Dolethal, Vetoquinol) followed by transcardial perfusion with 2.4% glutaraldehyde and 4% PFA in 0.1 M Na-cacodylate buffer. Optic nerves were gently dissected from the brain, while being immersed in fixative, followed by overnight post-fixation at 4 °C. Next, ascending concentrations of acetone were used to dehydrate the samples, after which they were placed in a 1:1 mixture of araldite epoxy resin and acetone overnight, and embedded in araldite expoxy resin. Next, 70 nm cross-sections of the optic nerves were made, transferred to 0.7% formvar-coated copper grids and contrasted with 0.5% uranyl acetate and lead citrate. Images were made with an EM208 S electron microscope (Philips), Morada soft imaging system camera and iTEM FEI software (Olympus). ImageJ software was used for morphometric analysis of at least 100 axons (on 4 different sections) per optic nerve. Axon area and axon-plus-myelin area were measured by encircling these areas, from which inner and out axon diameter, respectively, were calculated, as well as the g-ratio. Myelin area was calculated by subtracting the axon area from the axon-plus-myelin area. White space or interaxonal space was calculated by subtracting the sum of the axon-plus-myelin areas within a given region of interest from the total area of that region. Both measures are shown relative to the total region of interest (in %). Axon density was defined by counting the number of axons (Cell Counter plugin) in a 20×16 μm region of interest.

Statistical analysis

The employed statistical analyses and number of mice (N) or number of experiments performed (n) are stipulated in the respective figure legends. For experiments with OPCs/pmOLs, a minimum of three independent repeats, based on at least three different differentiation batches, was performed. Statistical analyses were performed using Prism v.8.2.1 (GraphPad). Differences were considered statistically significant for two-sided p-values < 0.05 (*$p < 0.05$; **$p < 0.01$; ***$p < 0.001$; ****$p < 0.0001$).

Results

Progressive vision loss and neuronal dysfunction in *Wfs1* knockout mice

Vision loss due to optic neuropathy is one of the main features of WS [77]. We therefore started with a comprehensive evaluation of visual function in the *Wfs1* KO mice. *Wfs1* KO mice indeed present with visual defects early in life: contrast sensitivity is reduced from the age of 3 months (Fig. 1a) and visual acuity declines starting at 6 months of age (Fig. 1b). Furthermore, electroretinograms showed that the amplitude of the positive scotopic threshold response progressively declined from 3 till 7.5 months of age in *Wfs1* KO mice (Fig. 1c and Figure S2), suggesting retinal ganglion cell dysfunction. A- and b-wave measurements were normal (Figure S2), indicating that specifically the retinal ganglion cells are primarily affected in the *Wfs1* KO mice. Next, visual evoked potential recordings also pointed to synaptic dysfunction and/or abnormal action potential conduction in the optic nerve, as evident from an age-dependent increase in the latency time of the visual evoked potentials (Fig. 1d and Figure S2). To directly assess axonal conduction properties of retinal ganglion cell axons, ex vivo compound action potential (CAP) recordings in the optic nerve were performed at the oldest age (7.5 months). No differences in the CAP peak latencies between the genotypes were observed (Fig. 1e-f), suggesting that action potential conduction speed is not overtly perturbed. However, when optic nerves were challenged with increasing stimulation frequencies, a more pronounced CAP peak decline at high frequencies was visible in *Wfs1* KO mice compared to WT littermates (Fig. 1g), suggesting an increase in conduction blocks when axons are required to fire at high rates. Notably, the post-stimulation CAP peak recovery kinetics appeared normal in *Wfs1* KO mice, implying that oligodendroglial potassium clearance is not overtly affected [39]. Finally, in vivo imaging of axonal transport in the optic nerve via manganese-enhanced MRI, showed an optic nerve diameter that tends to be smaller (with a significant difference at 6 months), and reduced innervation of the superior colliculus –i.e. reduction in the Mn^{2+}-labeled area of the superior colliculus after an intravitreal injection with Mn^{2+}– already at 3 months of age (Fig. 1h-i). Altogether, compared to WT littermates, *Wfs1* KO mice display an age-dependent deterioration of visual function, which culminates into progressive retinal ganglion cell dysfunction, higher susceptibility to activity-induced conduction blocks, and vision loss.

Analysis of the structural integrity of the retina, via in vivo optical coherence tomography revealed no apparent thinning nor swelling of the retinal layers in *Wfs1* KO *versus* WT mice (Fig. 1j). Immunohistological stainings at 7.5 months of age confirmed that there were no differences in the number of retinal ganglion cells (Fig. 1k) or dopaminergic amacrine cells (Fig. 1l) in the *Wfs1* KO mice compared to their WT littermates. Thus, despite the large body of evidence for neuronal dysfunction, we did not observe any signs of neurodegeneration in the retina of *Wfs1* KO mice up till the age of 7.5 months. Together, these data suggest that 7.5-month-old *Wfs1* KO mice are likely at the tipping point where WS pathological processes pose a stress on neuronal functionality but do not lead to overt neuronal death yet.

ER stress as potential underlying mechanisms of disease

As a potential underlying pathological mechanism of WS, we assessed ER stress. Western blotting showed increased levels of immunoglobulin heavy chain binding protein (BiP) (Fig. 2c-d) yet not of C/EBP homologous protein (CHOP) (Fig. 2e-f), in both retina and optic nerve lysates. This indicates that, while retinal cells in *Wfs1* KO mice do accumulate unfolded proteins in their ER lumen and launch an unfolded protein response (as evidenced by BiP), they do not display severe or unresolved ER stress (CHOP). Notably, the optic nerve was affected sooner (already at 3 months) than the retina (6 months).

Detailed analysis of the optic nerve suggests minor oligodendroglia defects

The central research question of this study is whether oligodendroglia may be the catalyzers of the neurodegeneration observed in WS. The observed increase in latency of the visual evoked potential recordings and the altered axonal conduction strength may be associated with myelin deficits. Hence, next, we further exploited the optic nerve to characterize in detail the oligodendroglia and myelin integrity in *Wfs1* KO *versus* WT mice. First, analysis of immunostainings on longitudinal optic nerve cryosections revealed equal numbers of OLIG2^{+} oligodendroglial cells (i.e., OPCs and oligodendrocytes) (Fig. 3b) and CC1^{+} mature oligodendrocytes at 7.5 months of age (Fig. 3c). However, cell counting of PDG-FRa[+] OPCs did show a reduced number of these cells in the optic nerve of *Wfs1* KO mice compared to WT controls (Fig. 3d). Analyses at younger ages indicate that this is not a developmental defect, but that this depletion
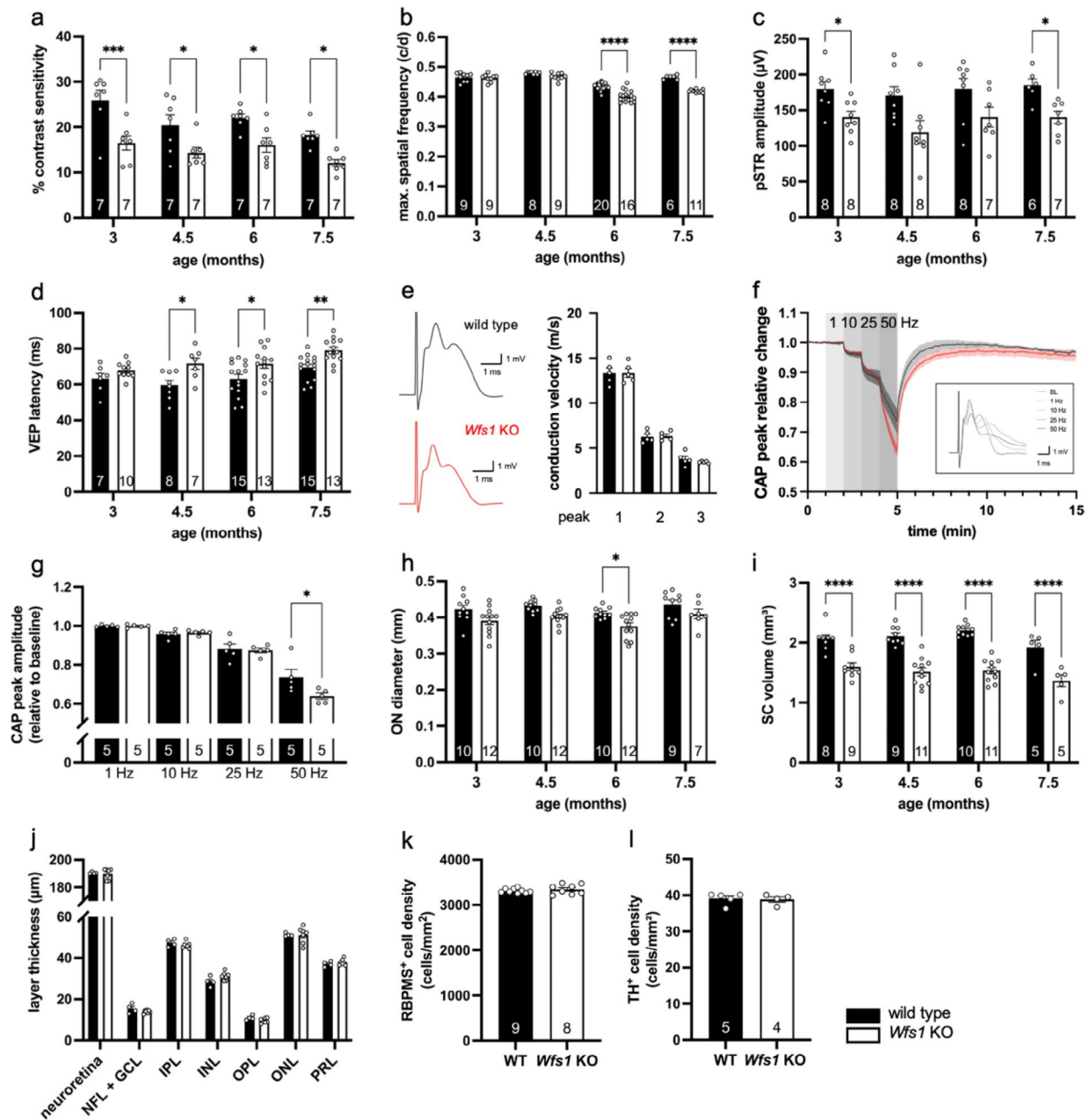
Fig. 1 Progressive vision loss and neuronal dysfunction yet no overt retinal neurodegeneration in *Wfs1* knockout mice. **a**, **b** Visual function is affected in *Wfs1* KO compared to WT mice, with contrast sensitivity (**a**) being affected earlier in life than visual acuity (**b**). Two-way ANOVA with Sidak's multiple comparisons; $F_{1,80}=65.04$ and $p<0.0001$ for genotype, $F_{3,80}=90.47$ and $p<0.0001$ for age, for contrast sensitivity; $F_{1,48}=40.33$ and $p<0.0001$ for genotype, $F_{3,48}=5.524$ and $p=0.0024$ for age, for visual acuity. **c** The amplitude of the positive scotopic threshold response is reduced in *Wfs1* KO mice. Mixed-effects analysis with Sidak's multiple comparisons; $F_{1,15}=18.46$ and $p=0.006$ for genotype, $F_{3,31}=1.006$ for age. **d** Latency of visual evoked potentials increases with age in *Wfs1* KO compared to WT mice. Two-way ANOVA with Sidak's multiple comparisons; $F_{1,80}=24.90$ and $p<0.0001$ for genotype, $F_{3,80}=6.720$ and $p=0.0004$ for age. **e** Representative CAP traces for wild type and *Wfs1* KO mice and the conduction velocity of the individual peaks at baseline (0.4 Hz). **f**, **g** Relative changes in peak amplitude, in response to increasing stimulation frequencies, show a larger CAP peak amplitude (P2) drop at 50 Hz in *Wfs1* KO nerves compared to WT (**g**). Unpaired t-test; $t_8=2.317$ and $p=0.0492$. **h-i** Mn^{2+-}enhanced MRI of the retinocollicular projection reveals a reduced optic nerve diameter (**h**) and superior colliculus innervation (**i**). Two-way ANOVA with Sidak's multiple comparisons; $F_{1,74}=21.41$ and $p<0.0001$ for genotype, $F_{3,74}=3.588$ and $p=0.0178$ for age, for optic nerve; $F_{1,60}=142.6$ and $p<0.0001$ for genotype, $F_{3,60}=3.331$ and $p=0.0253$ for age, for superior colliculus. **j** Analysis of the thickness of the retinal layers, as measured by optical coherence tomography, shows no differences between *Wfs1* KO and WT mice at 7.5 months of age. Multiple unpaired t-tests: $t_9=0,3632$ for neuroretina, $t_9=1,587$ for NFL+GCL, $t_9=1,137$ for IPL, $t_9=1,962$ for INL, $t_9=1,932$ for OPL, $t_9=0,07964$ for ONL, $t_9=0,9323$ for PRL. **k**, **l** Cell counts of retinal ganglion cells (**k**) and dopaminergic amacrine cells (**l**) reveal similar numbers in 7.5-month-old *Wfs1* KO and WT animals. Unpaired t-test; $t_{15}=20.8088$ for ganglion cells; $t_7=0.2544$ for amacrine cells. Data presented as mean±SEM, number of animals (N) depicted in the bar graphs
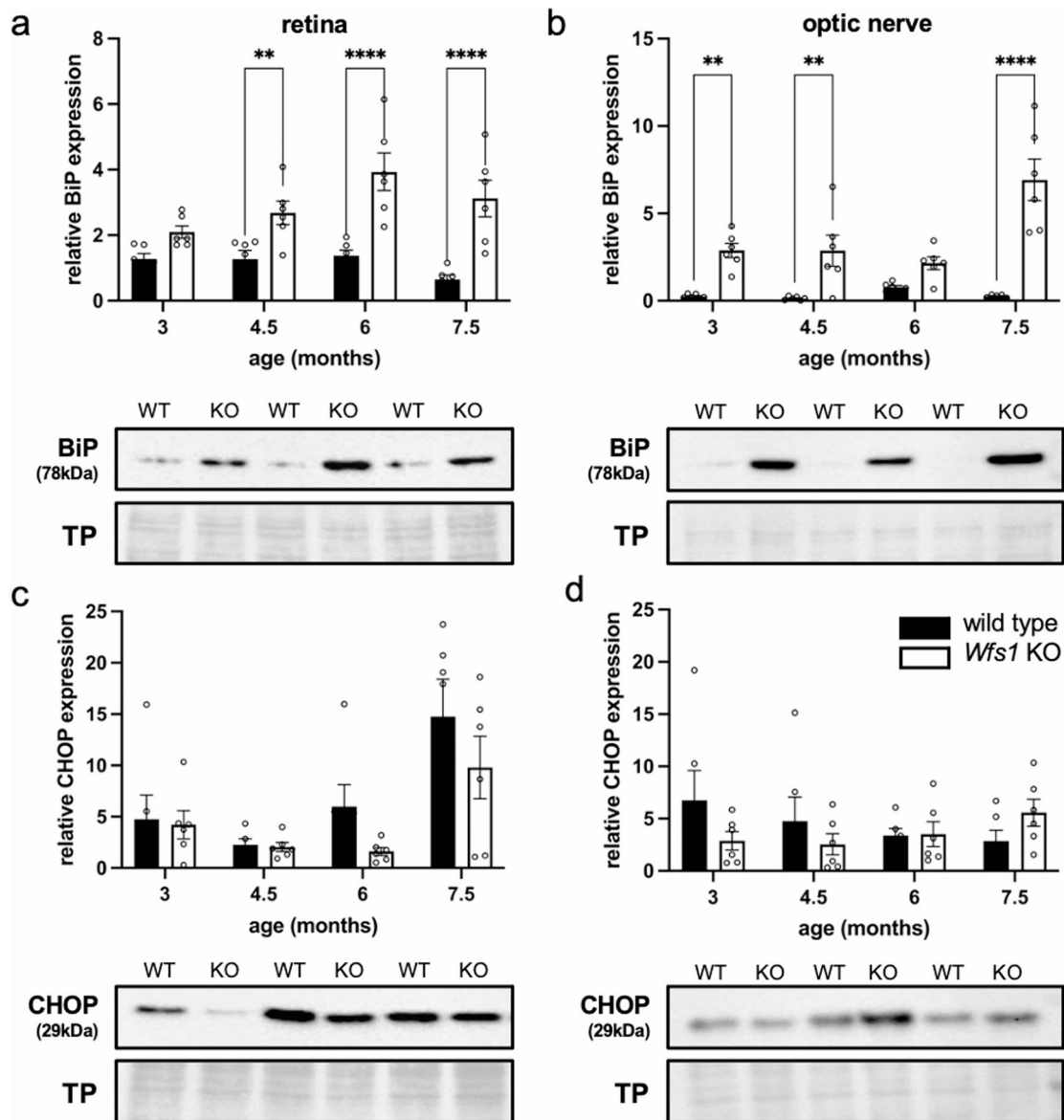
Fig. 2 Activation of the unfolded protein response but no unresolved ER stress in the retina and optic nerve of *Wfs1* KO mice. **a**, **b** Elevated BiP levels indicate that there is accumulation of unfolded proteins in the ER lumen in the retina (**a**) and optic nerve (**b**) of *Wfs1 KO* mice, but not of WT controls; starting from the age of 4.5 and 3 months, respectively. Two-way ANOVA with Sidak's multiple comparisons; $F_{1,40}=55.52$ and $p<0.0001$ for genotype, $F_{3,40}=2.992$ and $p=0.0421$ for age, with $p=0.0997$ for 3 months, $p=0.0061$ for 4.5 months, $p<0.0001$ for 6 months, $p<0.0001$ for 7.5 months, for retina; $F_{1,39}=67.94$ and $p<0.0001$ for genotype, $F_{3,39}=6.239$ and $p=0.0015$ for age, with $p=0.0022$ for 3 months, $p=0.0015$ for 4.5 months, $p=0.0956$ for 6 months, $p<0.0001$ for 7.5 months, for optic nerve. **c**, **d** CHOP expression levels are similar for both genotypes in the retina (**c**) and optic nerve (**d**). Two-way ANOVA with Sidak's multiple comparisons; $F_{1,39}=2.763$ for genotype, $F_{1,19}=8.846$ and $p=0.0036$ for age, for retina; $F_{1,10}=0.5544$ for genotype, $F_{3,30}=0.3121$ for age, for optic nerve. Data presented as mean $\pm$ SEM, $N=6$. TP: total protein stain

arises around the age of 6 months (Fig. 3d). Next, we determined the g-ratio of optic nerve axons on TEM images and found a higher g-ratio in the *Wfs1* KO mice –i.e., myelin thinning– at 7.5 months of age (Fig. 3e). This defect was subtle, as the average myelin area was similar for both genotypes (Fig. 3f). Furthermore, at this age, axon density, axon diameter and the empty space in between axons were identical in *Wfs1* KO and WT mice (Fig. 3g-i). Together, these findings suggest a complex

disease manifestation, with only late and subtle thinning of the myelin sheath and a reduction of the OPC pool, without any overt signs of axonal degeneration in the optic nerve.

The eye as a window to the brain
Although only minor morphological changes were apparent in the retina and optic nerve, structural neurodegeneration was detected in the brain of *Wfs1* KO mice
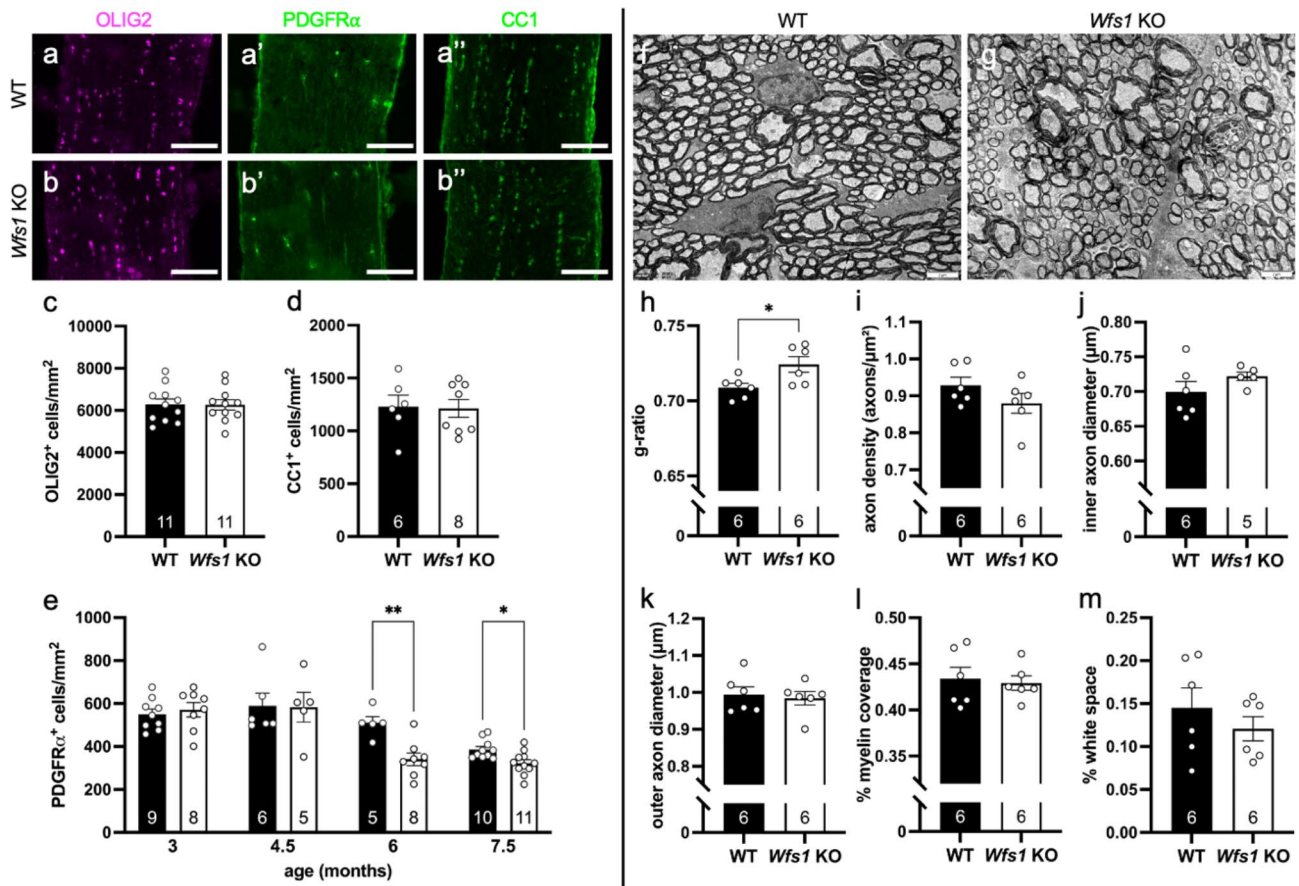
Fig. 3 A reduction in the number of OPCs and minor myelin defects in the *Wfs1* KO optic nerve. **a-e** Immunohistological stainings with different oligodendroglia lineage markers of WT (**a**) and *Wfs1* KO optic nerves (**b**) show equal cell numbers of OLIG2$^+$ oligodendroglial lineage cells (unpaired t-test, $t_{20}=0.05208$) (**c**), and CC1$^+$ mature oligodendrocytes (unpaired t-test, $t_{12}=0.1220$) (**d**); but a reduced number of PDGFRa$^+$ OPCs in *Wfs1* KO optic nerves compared to WT at 6 and 7.5 months of age (**e**). Mixed-effects analysis with Sidak's multiple comparisons; $F_{1,54}=5.512$ and $p=0.0226$ for genotype, $F_{2,27}=25.49$ and $p<0.0001$ for age; with $p=0.0092$ for WT *versus* Wfs1 KO at 6 months and $p=0.0317$ for WT *versus* Wfs1 KO at 7.5 months. **f-m** Transmission electron microscopy study of the optic nerve of 7.5-month-old WT (**f**) and *Wfs1* KO (**g**) mice reveals a difference between genotype for g-ratio (unpaired t-test, $t_{2.6}=10$, $p=0.0258$) (**h**), but not for axon density (unpaired t-test, $t_{1.4}=10$) (**i**), inner axon diameter (unpaired t-test, $t_{1.3}=9$) (**j**), outer axon diameter (unpaired t-test, $t_{0.3}=10$) (**k**), myelin area (unpaired t-test, $t_{0.3}=10$) (**l**) or empty space in between axons (unpaired t-test, $t_{0.9}=10$) (**m**). Scale bar 100 μm (a-b), 2 μm (f-g). Data presented as mean ± SEM, number of animals (N) depicted in the bar graphs

via MRI scans. In addition to shrinkage of superior colliculus volume and optic nerve diameter, as observed via Mn^{2+}-enhanced MRI (Fig. 1g-h), we observed more manifestations of neurodegeneration. First, MRI showed an overall reduction in brain volume (Fig. 4a), which likely correlates with the overall smaller posture of the *Wfs1* KO mice. Specific brain structures that were smaller in *Wfs1* KO mice compared to WT controls, after correction for smaller brain volume, were the brain stem (starting from 3 months) (Fig. 4b), cerebellum (starting from 4.5 months) (Fig. 4c) and superior colliculus (starting from 3 months) (Fig. 4d), but not olfactory bulb (Fig. 4e) nor cortex (Fig. 4f). Second, analysis of fractional anisotropy at the age of 7.5 months revealed significantly reduced values, indicative of reduced myelin integrity, in the medulla, pons, cerebellum and superior colliculus, but not in the corpus callosum, visual, motor or auditory

cortex (Fig. 4g). Decreased mean diffusivity values, also indicative of loss of structural integrity of myelin, were only observed in the cerebellum (Fig. 4h). In conclusion, these findings mirror the results from MRI studies performed in WS patients (reviewed in [68]) and point out that WS manifests as a disease affecting both grey and white matter of the brain stem, cerebellum and retinocollicular pathway.

Transcriptomics study of WS patient iPSC-derived oligodendrocytes

To generate more mechanistic insights into the contribution of oligodendroglia to WS pathology, we next investigated the function of these cells using WS patient-derived iPSCs as well as their isogenic controls that were differentiated into oligodendroglia. Creation of these engineered iPSC lines is described in supplement, and
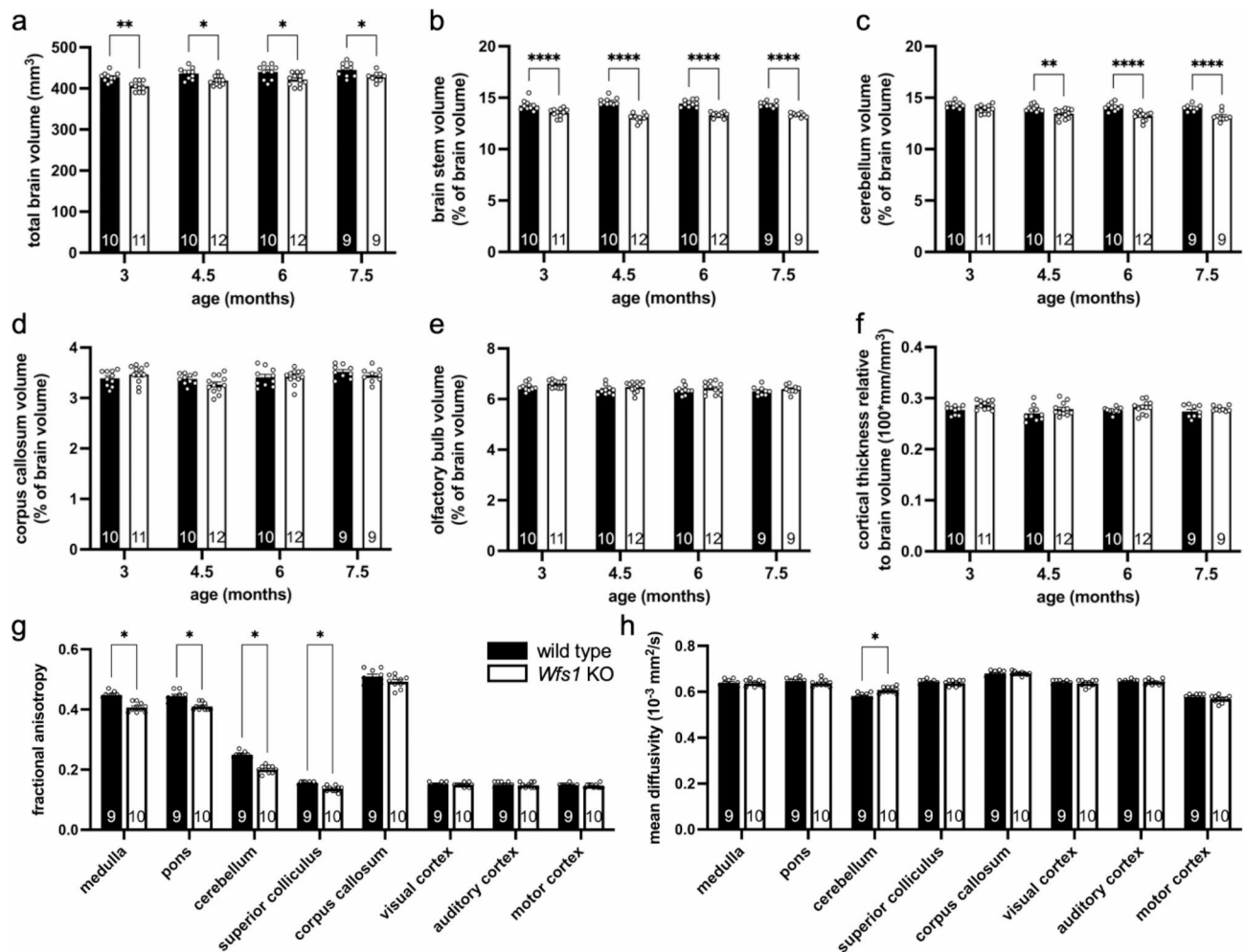
Fig. 4 White and grey matter loss in the brain of *Wfs1* KO mice. Structural MRI and diffusion tensor imaging study of *Wfs1* KO *versus* WT mice from age 3 till 7.5 months. **a** Total brain volume is reduced in *Wfs1* KO mice of all ages. Two-way ANOVA with Sidak's multiple comparisons; $F_{1,75}=37.23$ and $p<0.0001$ for genotype, $F_{3,75}=7.709$ and $p=0.0001$ for age, with $p=0.0015$ for 3 months, $p=0.0217$ for 4.5 months, $p=0.0108$ for 6 months, $p=0.0490$ for 7.5 months. **b** Brain stem volume of *Wfs1* KO animals is also reduced at all ages. Two-way ANOVA with Sidak's multiple comparisons; $F_{1,75}=203.2$ and $p<0.0001$ for genotype, $F_{3,75}=0.09256$ for age, with $p<0.0001$ *Wfs1* KO *versus* WT at all ages. **c** The volume of the cerebellum is smaller in *Wfs1* KO mice starting from 4.5 months. Two-way ANOVA with Sidak's multiple comparisons; $F_{1,75}=59.87$ and $p<0.0001$ for genotype, $F_{3,75}=6.754$ and $p=0.0004$ for age, with $p=0.0570$ for 3 months, $p=0.0085$ for 4.5 months, and $p<0.0001$ for 6 and 7.5 months. **d**, **f** The volume of the corpus callosum (**d**), olfactory bulb (**e**), and the thickness of the cortex (**f**) is similar between genotypes. Two-way ANOVA with Sidak's multiple comparisons; $F_{1,75}=0.5229$ for genotype, $F_{3,75}=3.910$ and $p=0.0119$ for age, for corpus callosum; $F_{1,75}=6.116$ and $p=0.0157$ for genotype, $F_{3,75}=4.160$ and $p=0.0088$ for age, for olfactory bulb; $F_{1,75}=9.389$ and $p=0.0030$ for genotype, $F_{3,75}=1.812$ for age, for cortical thickness. **g** Fractional anisotropy, studied in 7.5-month-old *Wfs1* KO and WT mice, is different between genotypes for medulla ($t_{17}=6.753$, $p=0.000024$), pons ($t_{17}=5.000$, $p=0.000548$), cerebellum ($t_{17}=9.618$, $p<0.000001$) and superior colliculus ($t_{17}=5.183$, $p=0.000449$), but not for corpus callosum ($t_{17}=1.705$), visual cortex ($t_{17}=0.7255$), auditory cortex ($t_{17}=0.7334$) nor motor cortex ($t_{17}=0.9602$). Multiple unpaired t-tests. **h** Mean diffusivity studied in 7.5-month-old *Wfs1* KO and WT mice, is different between genotypes only for cerebellum ($t_{17}=4.144$, $p<0.005416$). Multiple unpaired t-tests. Data presented as mean $\pm$ SEM, number of animals (N) depicted in the bar graphs

quality controls and characterization are shown in figures S3 to S5. First, we confirmed that oligodendroglia can be generated from *WFS1* mutant iPSCs by *SOX10* overexpression. Over the 24 days differentiation, we detected increasing transcript levels of *OLIG1*, *OLIG2* and *NKX2.2* lineage markers in *WFS1* mutant and isogenic iPSC progeny, and with >80% of the mutant and isogenic cells staining positive for O4 on DIV24 (Fig. 5a-f). A small proportion of these cells (~10%) also expressed MBP (Fig. 5c) and culturing these oligodendroglia on

electrospin fibers revealed MBP⁺ extensions on the fibers. Hence, we defined the day 24 iPSC progeny as a mixed population of OPCs and pmOLs.

Following confirmation that WFS1 expression levels were restored in both *WSF1* isogenic iPSCs [51] and OPCs/pmOLs (Figure S6), we performed a comparative transcriptomics study of the two pairs of WS patient iPSC-derived *versus* their isogenic control OPCs/pmOLs. A principal component analysis showed no clear clustering of patient line 1 and its isogenic control (Fig. 6a),
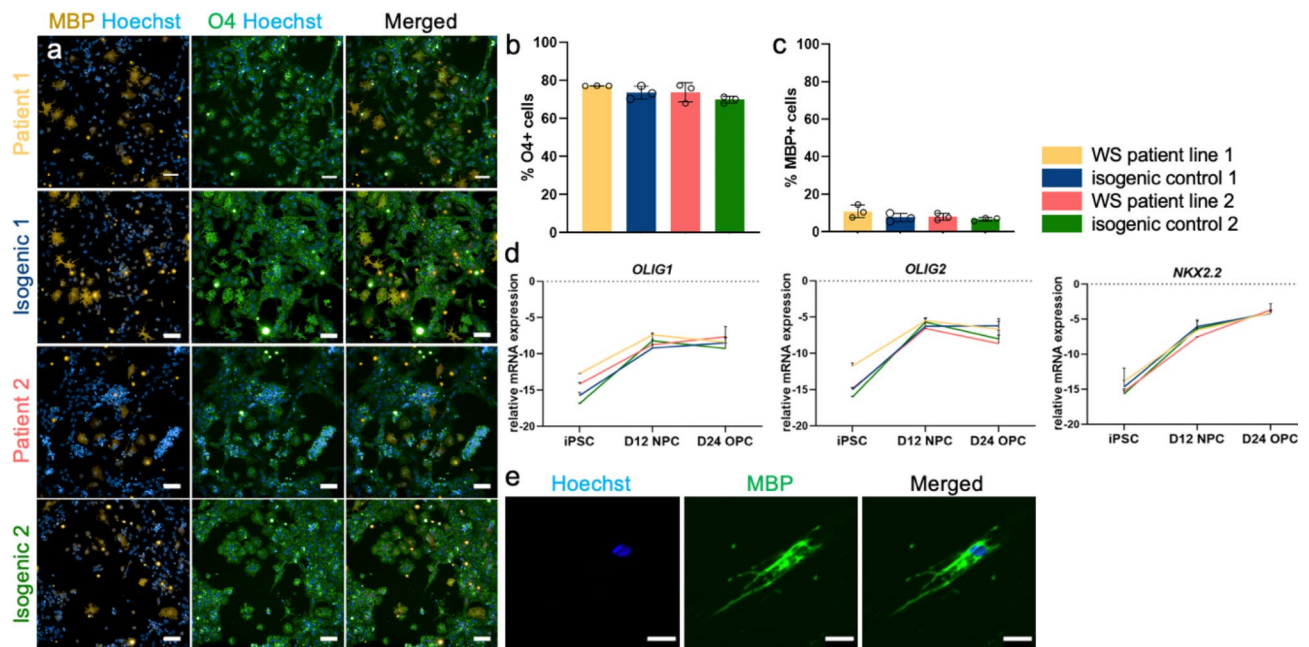
Fig. 5 Presence of WFS1 mutation does not affect iPSC-derived OPCs/pmOLs differentiation. **a** Immunocytochemistry for O4 and MBP on OPCs/pmOLs generated from WS patient iPSC lines 1 and 2, with their respective isogenic controls. Scale bar: 100 μm. **b-c** Quantification of the number of immunostained O4$^+$ (**b**) and MBP$^+$ cells (**c**) present at DIV24. **d** RT-qPCR for oligodendroglia lineage markers *OLIG1*, *OLIG2*, and *NKX2.2* throughout the OPC/pmOL differentiation of WS patient and isogenic lines. **e** Immunostaining for MBP on DIV24 oligodendroglia (23 days in vitro, DIV24) cultured on electrospinning fibers for two weeks. Scale bar: 25 μm. Unpaired t-test; $t_4 = 1.840$ for WS patient 1 vs. isogenic 1 and $t_4 = 1.268$ for WS patient 2 vs. isogenic 2, for O4; $t_4 = 1.406$ for WS patient 1 vs. isogenic 1 and $t_4 = 1.062$ for WS patient 2 vs. isogenic 2, for MBP. Data presented as mean ± SEM, $n = 3$ (a, c,d), $n = 1$ (e) and $n = 3$ (f)

and only 8 differentially expressed genes (adjusted p-value < 0.05) were found. These were mitochondrial genes (*MT-TA*, *MT-TF*, *MT-TH*, *MT-TK*, *MT-TM*, *MT-TN*) and *WFS1*, which were downregulated in the mutant cells, and *ZNF677*, of which the expression was upregulated (Fig. 6b). For patient line 2, clustering of the mutant *versus* isogenic control cells was observed (Fig. 6c) with a total of 895 differential transcripts (adjusted p-value > 0.05) (Fig. 6d). In both lines, oligodendrocyte lineage (*OLIG1*, *OLIG2*, *NKX2.2*) and differentiation (*RLBP1*, *PDGFRA*, *CSPG4*, *GPR17*, *CMIP2*, *PNPLA3*, *HAPLN2*, *APOD*) markers were not significantly altered in mutant *versus* isogenic OPCs/pmOLs, and, besides reduced *OMG* transcript levels in patient line 2, also expression of myelin components *MBP*, *MAG*, *PLP1*, *MOG* and *CNP* was similar. Furthermore, looking at transcripts with a link to known WS disease processes, in patient line 2, ER membrane was found twice in the top-5 cellular component GO terms, with genes connected to intracellular Ca^{2+} homeostasis and ER functions (*AKAP6*, *RYR2*, *CAMK2B*, *JPH4*). *RTN1*, encoding an ER-associated protein involved in neuroendocrine secretion and considered a specific marker for neurological disease, was found to be one of the most downregulated genes (Fig. 6e).

Remarkably, as seen previously in *WFS1* mutant cells [21, 22], several Serpin family members were upregulated, most prominently paralogs *SERPINE1* and *SERPINE2* (Fig. 6d). Besides their well-described role in blood coagulation, Serpins are also involved in preserving synaptic networks and their upregulation has been linked to several neurodegenerative diseases, including multiple sclerosis (MS) and amyotrophic lateral sclerosis (ALS). In line with known Serpin functions, pathways and processes connecting to morphogenesis and development, cell differentiation and cell fate commitment, as well as wound healing and blood coagulation, regulation of cell death/apoptosis, and extracellular matrix, were upregulated in patient line 2 (Fig. 6g).

Finally, in patient line 2, we observed that suppressed pathways in the mutant cells were mostly related to CNS development, synaptic signalling and regulation of neurotransmitter transport, with downregulated GO processes with a role in the cellular and molecular organisation of axo-glial synaptic junctions (Fig. 6h), and expression of the majority of the top-200 genes localising to neuronal compartments, synapse/synaptic vesicles, and cell junction (Fig. 6f).

Examining the human diseases that have been linked to the differentially expressed genes in this study, we found that many of the top-20 genes correlate with
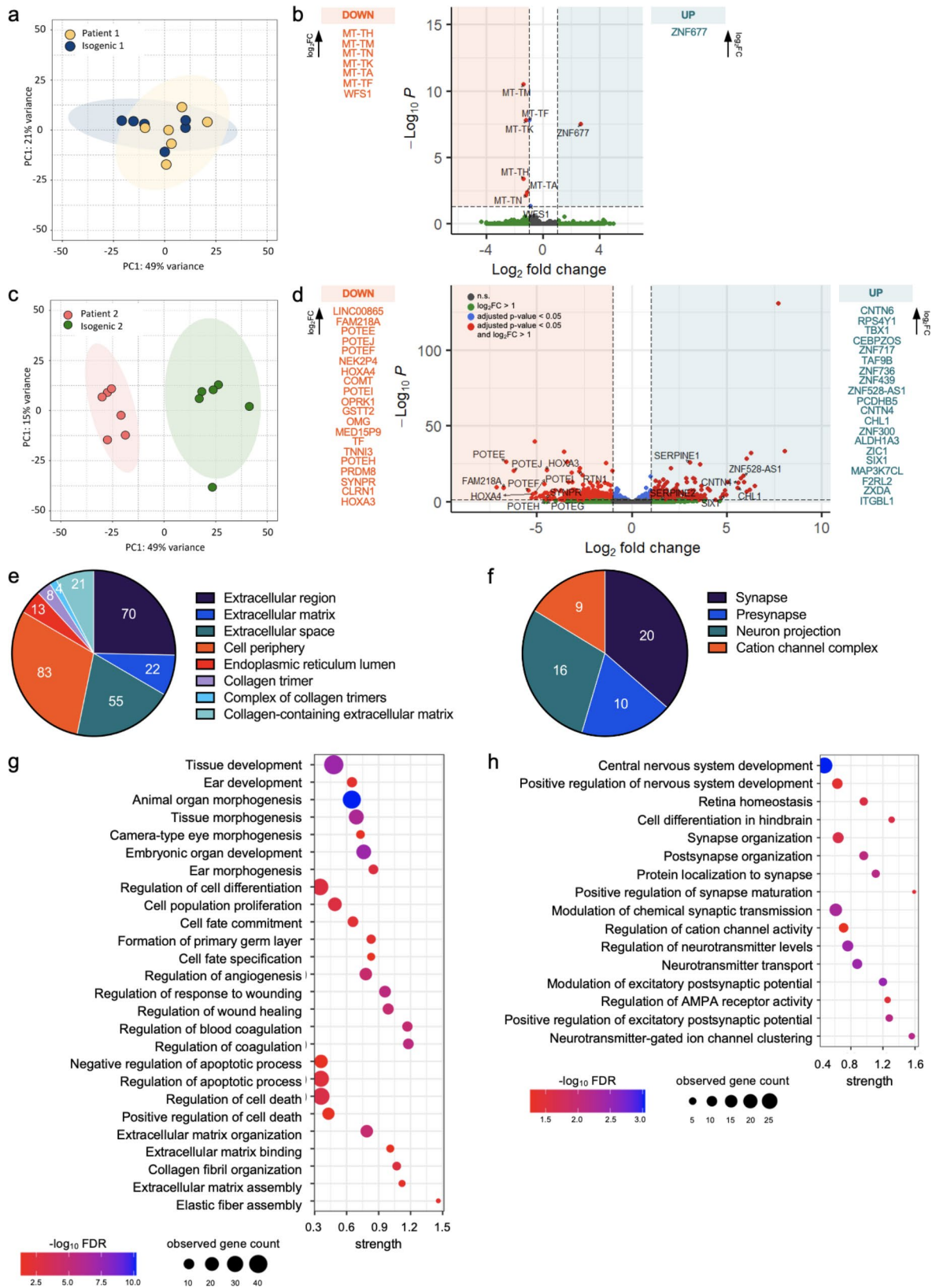
Fig. 6 (See legend on next page.)

(See figure on previous page.)

Fig. 6 Transcriptomics analysis of WS patient iPSC-derived OPCs/pmOLs and isogenic controls. **a** Principal component analysis of patient line 1 showing no distinct clustering. **b** Enhanced volcano plot showing differentially expressed genes for *WFS1* mutant *versus* isogenic control of patient line (1) Cut-off: adjusted p-value < 0.05 and log$_2$FC > 1. Downregulated genes are shown in orange, upregulated genes in blue; side panels show top-20 differentially expressed genes ranked based on log$_2$FC (highest at the top). **c** Principal component analysis of patient line 2 showing clustering of *WFS1* mutant *versus* isogenic control samples. **d** Enhanced volcano plot showing differentially expressed genes for *WFS1* mutant *versus* isogenic control of patient line (2) Cut-off: adjusted p-value < 0.05 and log$_2$FC > 1. Downregulated genes are shown in orange, upregulated genes in blue; side panels showing top-20 differentially expressed genes ranked based on log$_2$FC. **e-f** Functional enrichment analysis of differentially expressed genes in *WFS1* mutant OPCs/pmOLs from patient line 2. Pie charts show observed gene counts per GO Component for upregulated (**e**) and downregulated transcripts (**f**), to illustrate (sub) cellular localization of differentially expressed genes. **g-h** Functional enrichment analysis of differentially expressed genes in *WFS1* mutant OPCs/pmOLs from patient line 2, showing selected GO Processes associated with upregulated (**g**) and downregulated transcripts (**h**). $n = 6$

neurodevelopmental or neurodegenerative WS-like syndromes, characterized by hearing and/or vision loss, or diabetes. These include, in patient line 1, rare mitochondrial non-syndromic sensorineural deafness (*MT-TA, MT-TH, MT-TK, MT-TN, MT-TS1, MT-TW*), and, in patient line 2, Baraitser-Winter syndrome (*POTEE, POTEF, POTEG, POTEH, POTEI, POTEJ*), cone-rod dystrophy 13 (*FAM218A)*, Athabaskan brainstem dysgenesis syndrome (*HOXA3* and *HOXA4)*, nutritional optic neuropathy (*SYNPR)*, Cockayne syndrome A (*ZNF528-AS1)*, autosomal dominant deafness type 23 and branchio-otorenal spectrum disorder (*SIX1)*, and 3p deletion syndrome (*CNTN4* and *CHL1)*.

Taken together, in both patient lines, we found little evidence of differential expression of genes related to oligodendroglia function or within the oligodendroglia lineage cell compartment. Some differentially expressed genes localize to the mitochondria or ER, and play a role in intracellular Ca^{2+} homeostasis, ER and mitochondrial function, and can therefore be linked to cellular processes known to be affected in WS. Other differentially expressed genes have previously been linked to disorders bearing similarities with WS.

Mechanistic studies of WS disease processes in iPSC-derived oligodendroglia

Based on the results of the transcriptomics study, we next evaluated several cellular functions that have been linked to WS, and for which altered transcripts were found –mostly related to ER, in patient line 2. As delineated in the introduction, mutant WFS1 causes a typical MAM phenotype, associated with decreased ER Ca^{2+} stores, increased ER stress susceptibility, aberrant mitochondrial function, as well as defects in phosphatidylcholine generation from phosphatidylethanolamine –a lipid exchange and transport process that typically requires close contacts between the ER and mitochondria. We therefore assessed these different processes in the mutant and isogenic oligodendroglia. Accumulation of unfolded proteins and ER stress was assessed via RT-qPCR gene expression analysis of markers of the UPR pathway (*BiP, CHOP, IRE1a, ATF6* and *PERK*) in basal conditions as well as upon treatment with ER-stress inducers. To evoke ER stress, we opted to use thapsigargin, an irreversible

inhibitor of SERCA pumps thus depleting the ER Ca^{2+} stores, and tunicamycin, an inhibitor of the N-linked glycosylation of proteins, both resulting in the accumulation of unfolded proteins in the ER lumen. As anticipated, the addition of both thapsigargin and tunicamycin elevated the expression of ER stress markers (Fig. 7a), however, no significant differences were observed between mutant and isogenic control cells. Western blot analysis for BiP protein levels (with tunicamycin treatment) confirmed these data (Fig. 7b). Furthermore, an XBP1 splicing assay (with thapsigargin treatment) (Fig. 7c), measuring *bona fide* ER stress, also did not reveal an increased susceptibility to ER stress induction in WS patient compared to isogenic OPCs/pmOLs. Second, real-time cell metabolic analysis (Seahorse XF24, Agilent) disclosed unaltered mitochondrial function, with basal respiration, maximal respiration, ATP production, spare respiratory capacity and extracellular acidification rate unaltered in both pairs of mutant and isogenic oligodendroglia (Fig. 7d). Third, to assess ER-mitochondria interactions, we performed a quantitative analysis of MAMs with a proximity ligation assay using antibodies against vesicle-associated membrane protein-associated protein B (VAPB), on the ER membrane, and protein tyrosine phosphatase interacting protein 51 (PTPIP51), on the outer mitochondrial membrane, as previously used to identify a MAM phenotype in an iPSC model of ALS [85]. However, here, we did not identify any differences between mutant and isogenic iPSC-oligodendroglia (Fig. 7e-f). Normal functionality of the ER was further confirmed via intracellular Ca^{2+} measurements. ATP and acetylcholine were used to stimulate cell-surface receptors and thereby IP$_3$R-mediated Ca^{2+} release, which was detected by the Cal-520 dye as a Ca^{2+} sensor. No difference in terms of area under the curve and peak amplitudes (F$_{peak}$-F$_{baseline}$) was observed between the control and WS patient OPCs/pmOLs, thus indicating preserved Ca^{2+} storage in the ER (Fig. 8 and Figure S7). Finally, further confirming a preserved MAM phenotype, lipidomic profiling showed that no lipid classes were significantly different in WS *versus* isogenic oligodendroglia, including phosphatidylcholine, phosphatidylethanolamine and phosphatidylinositol (Figure S8) –which are among the phospholipids present in the mitochondrial membrane and typically affected in
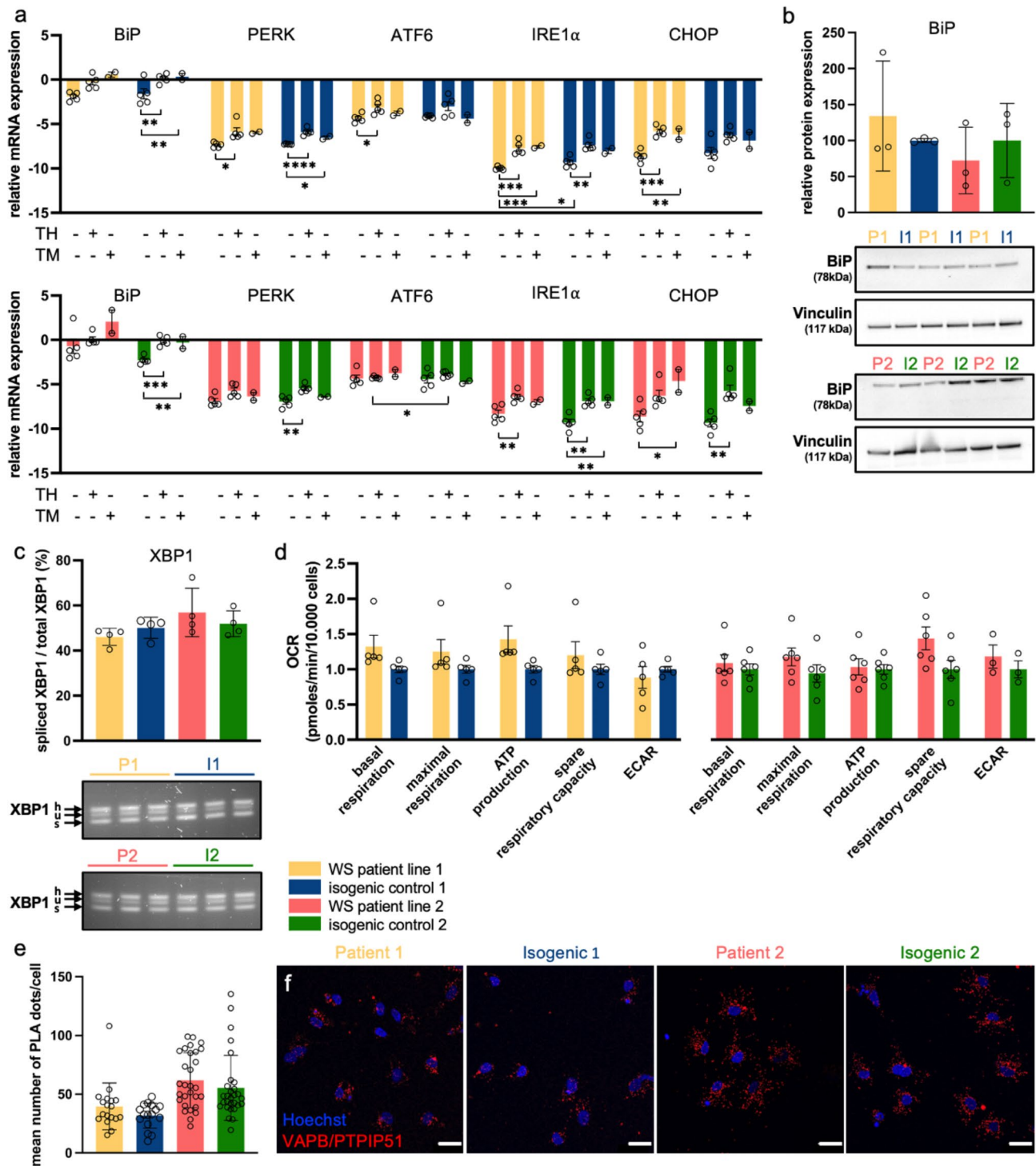
Fig. 7 (See legend on next page.)

case of a loss of MAMs. In summary, these experiments lead us to conclude that OPCs/pmOLs derived from WS patient iPSCs do not display any signs of ER abnormalities or chronic ER stress, mitochondrial dysfunction, or abnormal ER-mitochondria interactions. Albeit these cellular processes were previously found to be affected in pancreatic cells and neurons of WS patients, they appear to be functional in the OPCs/pmOLs studied here.

(See figure on previous page.)

Fig. 7 Mechanistic studies of WS disease processes in iPSC-derived OPCs/pmOLs. **a** RT-qPCR gene expression analysis of ER stress markers *BiP*, *PERK*, *ATF6*, *IRE1*α and *CHOP* in WS patient line 1 and 2, and their respective isogenic control OPCs/pmOLs, with/without ER stressors thapsigargin (TH) (2μM, 3 h) or tunicamycin (TM) (1 μg/ml, 24 h). **b** Protein expression levels of BiP (an indicator of unfolded protein accumulation in the ER lumen) after TM treatment in WS patient OPCs/pmOLs and isogenic controls (% relative to isogenic control). Unpaired t-test; $t_4 = 0.7714$ for WS patient 1 vs. isogenic 1 and $t_4 = 0.6923$ for WS patient 2 vs. isogenic 2. **c** Ratio of spliced to total XBP1 mRNA (an indicator of activation of the unfolded protein response) in WS patient OPCs and isogenic controls after TH treatment (2μM, 3 h). h: hybrid, s: spliced, u: unspliced XBP1 mRNA. Unpaired t-test; $t_6 = 1.324$ for WS patient 1 vs. isogenic 1 and $t_6 = 0.8214$ for WS patient 2 vs. isogenic 2. **d** Bioenergetic profile of mutant and isogenic control OPCs/pmOLs after addition of mitochondrial stressors, oligomycin, FCCP and rotenone. A Seahorse mitostress assay was performed to measure basal respiration, maximal respiration, ATP production, spare respiratory capacity, and extracellular acidification rate (ECAR). **e-f** Proximity ligation assay assessing proximity between ER (VAPB) and mitochondria (PTPIP51) in WS patient OPCs/pmOLs and isogenic controls, to evaluate MAM integrity. Unpaired t-test; $t_{32} = 1.401$ for WS patient 1 vs. isogenic 1 and $t_{56} = 0.9760$ for WS patient 2 vs. isogenic 2. Data presented as mean ± SEM. $n = 5$ for non-treated and TH, and $n = 2$ for TM (a), $n = 3$ (b), $n = 4$ (c), $n = 5$ for patient line 1 and $n = 3–6$ for patient line 2 (d), $n = 3$ with at least 16 images and $n > 100$ nuclei/condition (e). Scale bar 25 μm (f). Statistics for panel a and d are reported in supplementary table S2. P1: WS patient line 1, I1: isogenic line 1, P2: WS patient line 2, I2: isogenic line 2

Discussion

WS typically manifests as a combination of early-onset diabetes mellitus, progressive optic nerve atrophy, diabetes insipidus and sensorineural hearing loss. However, it is also associated with a number of neurological complications and psychiatric manifestations. Several studies have proven ER stress-mediated death of beta cells in WS, and therapeutic potential for diabetes medications such as glucagon-like peptide 1 receptor agonists [18, 48, 49]. In contrast, the disease mechanisms underlying the neurological and psychiatric manifestations of WS are less well understood, and recently oligodendrocytes have gotten increased attention. Indeed, similar to beta cells, by producing enormous amounts of plasma membrane during the myelination process, oligodendrocytes may be particularly susceptible to disruptions of the secretory pathway and ER stress [35]. Furthermore, beside myelinating axons, oligodendrocytes also support neuronal function and survival via metabolic coupling [39, 52]. ER stress in myelinating cells and loss of oligodendrocyte metabolic support have been shown to contribute to the pathogenesis of various demyelinating disorders, including MS, Charcot-Marie-Tooth disease, Pelizaeus-Merzbacher disease, vanishing white matter disease and ALS [35]. Similarly, for WS, a recent study by Rossi et al. found reduced monocarboxylate transporter 1 (MCT1) levels in the optic nerve of a WS mouse model, suggesting that the observed retinal neurodegeneration may in fact be caused by a lack of metabolic support from the oligodendrocytes. Furthermore, Samara et al. suggested that *WFS1* expression occurs predominantly in oligodendrocytes during early brain development [68]. This, together with neuroimaging studies showing abnormal white matter myelination in WS patients [42, 43, 69], led them to propose that WS could belong to a category of disorders characterized by ER stress-mediated myelination impairment [68]. Therefore, in this study, we aimed to better understand the role of oligodendroglia in WS pathogenesis and thereby lay the groundwork for the design of novel therapeutic strategies for neuroprotection in the WS CNS.

First, we found that *Wfs1* KO mice present with an age-dependent deterioration of visual function, starting from the age of 3 months and progressing to retinal ganglion cell dysfunction and impaired vision by the age of 7.5 months. Despite these overt functional deficits, we did not observe loss of retinal ganglion cells nor amacrine dopaminergic neurons in the retina of *Wfs1* KO mice up till the age of 7.5 months. This, combined with the unfolded protein response observed in the retina and optic nerve, suggests that we are looking at the earliest stages of disease, during which neuronal dysfunction is accumulating, but has not yet reached the tipping point towards cellular loss. Indeed, our findings confirm previous results in the same mouse model, in which neurodegeneration of the retinal ganglion cells was not seen at 8 months but manifested at 12 months [66], and mirror a study in WS patients, in which it was found that retinal ganglion cell axonal degeneration precedes cell body atrophy by about a decade [5]. Given the detrimental phenotype of this transgenic model, and applying humane end points, we limited our study to a maximum age of 7.5 months. At this age, we observed a mild and complex disease phenotype in the optic nerve, with alterations in axonal conduction strength combined with subtle thinning of the myelin sheath and a reduction of the OPC pool. Again, these findings are in line with a previous study in this *Wfs1*$^{\Delta exon8}$ mouse model [66], as well as in *Wfs1*$^{\Delta exon2}$ mouse and *Wfs1*$^{\Delta exon5}$ rat models [8, 58]. Novel findings in our study originate from ex vivo measurements of optic nerve CAPs, which allowed us to investigate a potential defect in the optic nerve while excluding the retinal ganglion cell bodies and synapses. These experiments uncovered a higher susceptibility to activity-induced conduction blocks in axons of *Wfs1* KO mice. These changes in axonal spiking capacity may arise from elevated K$^+$ accumulation during firing or energy deficits in the axons. However, the speed of CAP peak recovery following high-frequency stimulation indicates that oligodendroglia potassium clearance [39] is not overtly affected in *Wfs1* KO animals.

Overall, the phenotype of the retina and optic nerve of the *Wfs1* KO mouse recapitulates one of the disease
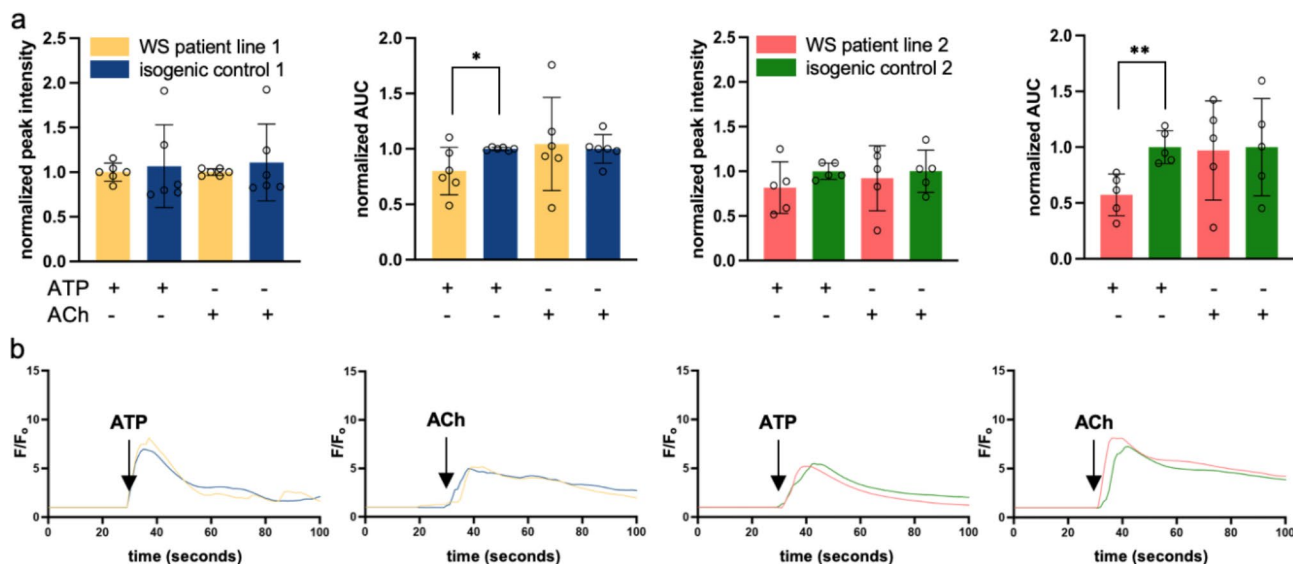
Fig. 8 Mechanistic studies of WS disease processes in iPSC-derived OPCs/pmOLs (continued). **a** Quantification of cytosolic Ca^{2+} release by WS patient and isogenic OPCs/pmOLs after pharmacological activation of IP_3R-mediated Ca^{2+} release by addition of 10 µM ATP or 10 µM acetylcholine (ACh) to the culture medium. **b** Average traces of cytosolic Ca^{2+} release by WS patient and isogenic OPCs/pmOLs after pharmacological activation of IP_3R-mediated Ca^{2+} release. Data presented as mean ± SEM. $n=6$ for patient line 1 and $n=5$ for patient line 2. Statistics are reported in supplementary table S3

hallmarks of WS, i.e., optic neuropathy. Furthermore, the MRI study conducted in these mice confirms that the eye is a window to the brain and that manifestations of the disease in the brain stem, cerebellum and retinocollicular pathway recapitulate findings in WS patients (reviewed in [68]). Reduced volumes of the total brain, brainstem and cerebellum, as well as reduced fractional anisotropy values in the medulla, pons, cerebellum and superior colliculus, indicate that both grey and white matter are affected in the WS brain, and corroborate a myelin or oligodendrocyte defect.

Second, to further interrogate oligodendroglia function and assess whether any cell intrinsic defects may lead to primary oligodendroglia dysfunction and thereby increase vulnerability of the neurons, we performed a detailed and comprehensive assessment of cellular processes potentially affected in WS. Two pairs of *WFS1* mutant OPCs/pmOLs with concomitant isogenic controls were studied. A comparative transcriptomics study revealed that the transcriptome of the WS patient-derived OPCs/pmOLs was divergent, with few –mostly mitochondrial– differentially expressed genes in patient line 1, and patient line 2 having differentially expressed genes localising to the ER. This may reflect the phenotypic heterogeneity of the more than 200 mutations of the *WFS1* gene that have been described as causing the disease [54] and suggests that future studies should include several mutant cell lines/models. However, a comprehensive set of in vitro studies showed that these rather limited transcriptional changes do not translate into a MAM phenotype, as has been described for mutant *WFS1* neurons [9, 13, 56, 83] and the *Wfs1^{E864K}* mouse

[56]. Specifically, the ER-mitochondria interactions, as measured with a proximity assay, were similar between mutant and isogenic oligodendroglia, and this was associated with normal phosphatidylcholine, phosphatidyletha-nolamine, and phosphatidylinositol levels. Furthermore, normal ER Ca^{2+} storage, no increased ER stress susceptibility, and normal mitochondrial activity were observed. These findings in our OPC/pmOL cultures thus contrast with previous studies in WS patient iPSC-derived neurons, which reported a crucial role for in Ca^{2+} dynamics at the MAMs, leading to mitochondrial bioenergetic deficits [13, 56]. Indeed, specifically in WS patient iPSC-derived neurons, aberrant neurite outgrowth due to an ATF6-mediated unfolded protein response was reported, [59] as well as a causal link between loss and mitochondrial dysfunction, including compromised mitochondrial respiration, reduced ATP production, mitochondrial depolarization and increased oxidative stress [84].

Other observations from the transcriptomics study include that both *WFS1* mutant cell lines had several top differentially expressed genes with a role in retinal homeostasis and associated with developmental disorders bearing striking similarities to WS, including syndromes with congenital deafness and retinal/optic nerve atrophy. Furthermore, two gene paralogs were found to be upregulated in patient line 2, namely *SERPINE1* and *SERPINE2*, and previous transcriptomics studies of pancreatic islets [21] and hippocampus and hypothalamus [22] of WFS1-deficient mice also revealed upregulated *SERPINA7* and *SERPINA10.* In the CNS, these serine protease inhibitors play roles that extend beyond their well-known function as inhibitors of fibrinolysis.

SERPINE1 may play a role in neurodegeneration/neuroprotection via extracellular matrix remodelling, excitotoxicity, blood-brain barrier opening, and recruitment and activation of microglia [31], while secretion of SERPINE2 by astroglia/oligodendroglia at the axoglial junction is believed to regulate nodal length and myelin structure in the optic nerve and corpus callosum [14]. Aberrant expression of *SERPINE1* has been linked to neurodegenerative diseases, including Alzheimer's [1, 29], Parkinson's disease [63], and MS [31]. Serpinopathies, e.g., ALS (with SERPINE2 accumulation), are characterized by neuronal inclusion bodies that accumulate within the ER and elicit an ER overload response and cell death signalling, [10, 31, 46, 57]. *SERPINE1* and *SERPINE2* thus seem to be nodes connecting the pathways related to morphogenesis and development, wound healing and blood coagulation, regulation of cell death/apoptosis, and extracellular matrix, and even ER stress, that were observed to be differentially expressed in our transcriptomics analyses. Importantly, it has been proposed that targeting of SERPINs may constitute a clinically-relevant molecular approach to the therapy of neurodegenerative diseases associated with increased SERPIN levels [29]. Altogether, our transcriptomics analysis revealed differential expression of several disease-relevant targets. However, these transcriptional changes appeared not to result in a detrimental phenotype, as the cellular assays did not reveal any abnormalities in cellular functions known to be compromised in WS.

One striking yet also still puzzling finding from the transcriptomics study, is the large number of transcripts related to neuronal compartments, synapse, (synaptic) vesicles, and cell junction, and suppressed genes and gene networks that may be linked to axo-glial synaptic junctions. OPCs form synaptic complexes with neurons, and detect neuronal activity through various neurotransmitter receptors and ion channels [76]. At these axo-glial synapses, glutamate and GABA signaling play crucial roles in regulating OPC proliferation, oligodendrocyte maturation, and myelin formation [6, 27, 76, 86, 87]. Downregulated gene networks in the WS patient iPSC-derived OPCs/pmOLs, related to synapse maturation and ion channel clustering, suggest compromised axo-glial synaptic junctions. This bidirectional communication between neurons and oligodendroglia impacts OPC motility, proliferation, oligodendrocyte maturation, myelination, metabolic support for axons, and remyelination [50, 76]. One may speculate that the observed depletion of the OPC pool and abnormal myelin wrapping in 7.5-month-old *Wfs1* KO mice could be the result from abnormal neuron-OPC interactions. Notably, impaired synapse formation and function has been observed in *WFS1*-deficient cerebral organoids, together with neuronal loss. An association with reduced

astrocytes was found, yet oligodendroglia were not studied [81].

The importance of neuron-glia communication points out one of the limitations of the current study, namely that we used monocultures of OPCs/pmOLs. Future studies with bi- or triculture systems of neurons, oligodendrocytes, and preferably also astrocytes, or organoids, are needed to study intercellular interactions in WS. These experiments are essential to clarify the cellular and molecular processes that, despite relatively normal cellular functions in the OPCs/pmOLs, lead to neuronal loss in WS. In this respect, it is also a drawback that we did not assess the phenotype of neurons differentiated from the WS patient iPSC lines used in this study. Another limitation may be that we used a population of oligodendrocyte lineage cells, of which only a small proportion expresses low levels of MBP and forms MBP$^+$ extensions on electrospin fibers. These cells were defined as a mixed population of OPCs and pmOLs. Prolonged maturation up till 8–10 weeks, together with an axon or axon-like substrate for myelination, would be required for these cells to become mature, myelinating oligodendrocytes. As such, we cannot make any claims about a primary involvement of mature oligodendrocytes in WS, nor study processes related to myelination. Notably, the used OPCs/pmOLs are also likely to be less prone to ER stress as compared to myelinating oligodendrocytes. However, this disadvantage may have turned into a strength, and led to evidence for a role for OPCs rather than for fully mature oligodendrocytes at the axo-glial synapse. Intriguingly, further supporting the importance of OPCs for CNS function, neuronal loss was rescued and lactate production/release was restored in iPSC-derived motor neurons from ALS patients, by knockdown of the disease-causing gene *SOD1* in OPCs but not by knockdown in mature oligodendrocytes [15]. This underscores the importance of oligodendrocyte-lineage cells, especially OPCs, in neurodegeneration, and should be an incentive to further explore OPC proliferation, survival and differentiation dynamics in WS.

A rational implementation of future WS therapies requires a cell type-specific understanding of the disease. The research question of this study, namely whether oligodendrocyte dysfunction may be the primary cause of the disease, was prompted by the rising interest in gene therapy as a treatment for WS neurodegeneration [47]. Although the current study did not lead to a conclusive answer, its results form a basis for future preclinical research. We have shown that the anatomical organization of the retina and optic nerve, together with available techniques for in vivo monitoring of retinal structure, axonal conductance and neural circuit connectivity, and visual function, allows to specifically interrogate neuronal *versus* oligodendroglia functionality. This, together with

Ahuja *et al. Acta Neuropathologica Communications* (2024) 12:140

Page 20 of 23

the accessibility and advantages of the eye for preclinical research –such as the small volume of the vitreous cavity, which may serve as a reservoir for local drug delivery–, makes the mouse visual system a valuable model to assess future therapeutic neuroprotective or -restorative strategies for WS. Additionally, vision loss is one of the defining hallmarks of WS and a major determinant of quality of life. As confirmed by the MRI findings in this study, and given that the retina and optic nerve are an integral part of the CNS, we expect that findings can be extrapolated to the rest of the CNS and that a proof-of-concept study in the retina/optic nerve will be a first step in the application of gene therapy to other brain regions such as the brain stem and cerebellum.

Conclusions

Following studies of the neurodegenerative phenotype of rodent WS models and WS patient iPSC-derived neurons, in this study, we focused on potential intrinsic defects in the oligodendroglia as a major contributor to WS pathogenesis. Our neuropathological and molecular findings suggest that cellular functions in *Wfs1* KO mouse oligodendrocytes and WS patient iPSC-derived OPCs/pmOLs are largely conserved. Given the cellular defects that have been previously observed in neurons in WS, and incentivised by the transcriptomic changes in the OPCs/pmOLs that may affect OPC-neuron synaptic junctions, and a depleted OPC pool in the optic nerve of *Wfs1* KO mice, we propose that future research should address neuron-glia communication to come to a better understanding of the pathogenesis of WS.

Abbreviations

ALS	amyotrophic lateral sclerosis
BiP	immunoglobulin heavy chain binding protein
CAP	compound action potentials
CHOP	C/EBP homologous protein
CNS	central nervous system
DAPI	4′,6-diamidino-2-phenylindole
EAAT2	excitatory amino acid transporter 2
ER	endoplasmic reticulum
GFAP	glial fibrillary acidic protein
IBA1	ionized calcium-binding adaptor molecule 1
iPSC	induced pluripotent stem cell
MAMs	mitochondria-associated endoplasmic reticulum membranes
MBP	myelin basic protein
MCT1	monocarboxylate transporter 1
MS	multiple sclerosis
OMM	oligodendrocyte maturation medium
OPCs	oligodendrocyte precursor cells
PDGFRa	platelet-derived growth factor receptor alpha
PFA	paraformaldehyde
PLA	proximity ligation assay
pmOLs	pre-myelinating oligodendrocytes
PTPIP51	protein tyrosine phosphatase interacting protein 51
RBPMS	RNA-binding protein with multiple splicing
ROI	region of interest
TBST	Tris-buffered saline with Tween-20
TH	thapsigargin
TM	tunicamycin
VAPB	vesicle-associated membrane protein B
WFS1	Wolfram syndrome 1, wolframin
WS	Wolfram syndrome
XBP1	X-Box-Binding protein 1

Supplementary Information

The online version contains supplementary material available at https://doi.org/10.1186/s40478-024-01851-7.

> Supplementary Material 1
>
> Supplementary Material 2

Data availability

The transcriptomics datasets generated and analysed during the current study are available in the GEO repository [GSE264222]. The lipidomics dataset is included as a supplement. All other datasets are available from the corresponding author on reasonable request.

Declarations

Ethics approval and consent to participate

All animal experiments were performed according to the European directive 2010/63/EU and approved by the KU Leuven institutional ethics committee for animal research (project no. P068/2018). All human iPSC studies were done after approval by the KU Leuven institutional ethics committee (project no. S50354).

Consent for publication

Not applicable.

Competing interests

The authors declare that they have no competing interests.

Author details

[1]Cellular Communication and Neurodegeneration Research Group, Animal Physiology and Neurobiology Division, Department of Biology, Leuven Brain Institute, KU Leuven, Leuven, Belgium
[2]Neural Circuit Development and Regeneration Research Group, Animal Physiology and Neurobiology Division, Department of Biology, Leuven Brain Institute, KU Leuven, Leuven, Belgium

³Stem Cell Institute, Department of Development and Regeneration, KU Leuven, Leuven, Belgium

⁴Laboratory of Molecular and Cellular Signalling, Department of Cellular and Molecular Medicine, Leuven Cancer Institute, KU Leuven, Leuven, Belgium

⁵Department of Neurosciences, Experimental Neurology and Leuven Brain Institute, KU Leuven, Leuven, Belgium

⁶VIB Center for Brain & Disease Research, Laboratory of Neurobiology, VIB-KU Leuven, Leuven, Belgium

⁷Institute of Pharmacology and Toxicology, Neuroscience Center Zurich, University of Zurich, University and ETH Zurich, Zurich, Switzerland

⁸Biomedical MRI Group/MoSAIC, Department of Imaging and Pathology, KU Leuven, Leuven, Belgium

⁹Laboratory Animal Centre, Institute of Biomedicine and Translational Medicine, University of Tartu, Tartu, Estonia

¹⁰Laboratory for Cell Death Research & Therapy, Department of Cellular and Molecular Medicine, Leuven Center for Cancer Biology, VIB-KU, Leuven Cancer Institute, VIB-KU Leuven, Leuven, Belgium

¹¹Laboratory of Lipid Metabolism and Cancer, Department of Oncology, Leuven Cancer Institute, KU Leuven, Leuven Institute for Single Cell Omics (LISCO), KU Leuven, Leuven, Belgium

¹²Laboratory for Functional Imaging and Research on Stem Cells, BIOMED, UHasselt – Hasselt University, Diepenbeek, Belgium

References

1. András IE, Serrano N, Djuraskovic I, Fattakhov N, Sun E, Toborek M (2023) Extracellular vesicle-Serpine-1 affects neural progenitor cell mitochondrial networks and synaptic density: modulation by amyloid Beta and HIV-1. Mol Neurobiol 60:6441–6465. https://doi.org/10.1007/s12035-023-03456-y
2. Andrews S (2010) FastQC: a quality control tool for high throughput sequence data. http://www.bioinformatics.babraham.ac.uk/projects/fastqc
3. Angebault C, Fauconnier J, Patergnani S, Rieusset J, Danese A, Affortit CA, Jagodzinska J, Mégy C, Quiles M, Cazevieille C al (2018) ER-mitochondria cross-talk is regulated by the Ca2 + sensor NCS1 and is impaired in Wolfram syndrome. Science signaling, City, p eaaq1380
4. Aronesty E (2011) ea-utils: command-line tools for processing biological sequencing data https://github.com/ExpressionAnalysis/ea-utils
5. Barboni P, Amore G, Cascavilla ML, Battista M, Frontino G, Romagnoli M, Caporali L, Baldoli C, Gramegna LL, Sessagesimi Eet al et al (2022) The pattern of retinal ganglion cell loss in Wolfram Syndrome is distinct from mitochondrial Optic neuropathies. Am J Ophthalmol 241:206–216. https://doi.org/10.1016/j.ajo.2022.03.019
6. Bergles DE, Roberts JD, Somogyi P, Jahr CE (2000) Glutamatergic synapses on oligodendrocyte precursor cells in the hippocampus. Nature 405:187–191. https://doi.org/10.1038/35012083
7. Bespalova IN, Van Camp G, Bom JH, Brown S, Cryns DJ, DeWan K, Erson AT, Flothmann AE, Kunst K, Kurnool Pet al et al (2001) Mutations in the Wolfram syndrome 1 gene (WFS1) are a common cause of low frequency sensorineural hearing loss. Hum Mol Genet 10:2501–2508. https://doi.org/10.1093/hmg/10.22.2501
8. Bonnet Wersinger D, Benkafadar N, Jagodzinska J, Hamel C, Tanizawa Y, Lenaers G, Delettre C (2014) Impairment of visual function and retinal ER stress activation in Wfs1-Deficient mice. PLoS ONE 9:e97222. https://doi.org/10.1371/journal.pone.0097222
9. Cagalinec M, Liiv M, Hodurova Z, Hickey MA, Vaarmann A, Mandel M, Zeb A, Choubey V, Kuum M, Safiulina D et al (2016) Role of Mitochondrial Dynamics in Neuronal Development: Mechanism for Wolfram Syndrome. PLoS Biol 14: e1002511 https://doi.org/10.1371/journal.pbio.1002511
10. Chou SM, Taniguchi A, Wang HS, Festoff BW (1998) Serpin = serine protease-like complexes within neurofilament conglomerates of motoneurons in amyotrophic lateral sclerosis. J Neurol Sci 160(1):S73–79. https://doi.org/10.1016/s0022-510x(98)00202-0
11. Claes M, Santos JRF, Masin L, Cools L, Davis BM, Arckens L, Farrow K, De Groef L, Moons L (2021) A Fair Assessment of evaluation tools for the murine microbead occlusion model of Glaucoma. Int J Mol Sci 22. https://doi.org/10.3390/ijms22115633
12. Delpech J-C, Pathak D, Varghese M, Kalavai SV, Hays EC, Hof PR, Johnson WE, Ikezu S, Medalla M, Luebke Jl al (2021) Wolframin-1–expressing neurons in the entorhinal cortex propagate tau to CA1 neurons and impair hippocampal memory in mice. Sci Transl Med 13:eabe8455. https://doi.org/10.1126/scitranslmed.abe8455
13. Delprat B, Maurice T, Delettre C (2018) Wolfram syndrome: MAMs' connection? Cell Death Dis 9:364. https://doi.org/10.1038/s41419-018-0406-3
14. Dutta DJ, Woo DH, Lee PR, Pajevic S, Bukalo O, Huffman WC, Wake H, Basser PJ, SheikhBahaei S, Lazarevic V et al (2018) Regulation of myelin structure and conduction velocity by perinodal astrocytes. Proc Natl Acad Sci U S A 115: 11832–11837 https://doi.org/10.1073/pnas.1811013115
15. Ferraiuolo L, Meyer K, Sherwood TW, Vick J, Likhite S, Frakes A, Miranda CJ, Braun L, Heath PR, Pineda R et al (2016) Oligodendrocytes contribute to motor neuron death in ALS via SOD1-dependent mechanism. Proc Natl Acad Sci U S A 113: E6496-e6505 https://doi.org/10.1073/pnas.1607496113
16. Fonseca SG, Fukuma M, Lipson KL, Nguyen LX, Allen JR, Oka Y, Urano F (2005) WFS1 is a novel component of the unfolded protein response and maintains homeostasis of the endoplasmic reticulum in pancreatic beta-cells. J Biol Chem 280:39609–39615. https://doi.org/10.1074/jbc.M507426200
17. Garcia-Leon JA, Kumar M, Boon R, Chau D, One J, Wolfs E, Eggermont K, Berckmans P, de Gunhanlar N Vrij F et al (2018) SOX10 Single Transcription Factor-Based Fast and Efficient Generation of Oligodendrocytes from Human Pluripotent Stem Cells. Stem cell reports 10: 655–672 https://doi.org/10.1016/j.stemcr.2017.12.014
18. Gorgogietas V, Rajaei B, Heeyoung C, Santacreu BJ, Marín-Cañas S, Salpea P, Sawatani T, Musuaya A, Arroyo MN, Moreno-Castro Cet al et al (2023) GLP-1R agonists demonstrate potential to treat Wolfram syndrome in human preclinical models. Diabetologia 66:1306–1321. https://doi.org/10.1007/s00125-023-05905-8
19. Hershey T, Lugar HM, Shimony JS, Rutlin J, Koller JM, Perantie DC, Paciorkowski AR, Eisenstein SA, Permutt MA, Washington University Wolfram Study G (2012) Early brain vulnerability in Wolfram syndrome. PLoS ONE 7:e40604. https://doi.org/10.1371/journal.pone.0040604
20. Hofmann S, Philbrook C, Gerbitz KD, Bauer MF (2003) Wolfram syndrome: structural and functional analyses of mutant and wild-type wolframin, the WFS1 gene product. Hum Mol Genet 12:2003–2012
21. Ivask M, Hugill A, Kõks S (2016) RNA-sequencing of WFS1-deficient pancreatic islets. Physiol Rep 4. https://doi.org/10.14814/phy2.12750
22. Ivask M, Pajusalu S, Reimann E, Kõks S (2018) Hippocampus and hypothalamus RNA-sequencing of WFS1-deficient mice. Neuroscience 374:91–103. https://doi.org/10.1016/j.neuroscience.2018.01.039
23. Kim D, Paggi JM, Park C, Bennett C, Salzberg SL (2019) Graph-based genome alignment and genotyping with HISAT2 and HISAT-genotype. Nat Biotechnol 37:907–915. https://doi.org/10.1038/s41587-019-0201-4
24. Kõks S (2023) Genomics of Wolfram Syndrome 1 (WFS1). Biomolecules 13. https://doi.org/10.3390/biom13091346
25. Kõks S (2023) Genomics of Wolfram Syndrome 1 (WFS1). Biomolecules 13:1346
26. Kõks S, Overall RW, Ivask M, Soomets U, Guha M, Vasar E, Fernandes C, Schalkwyk LC (2013) Silencing of the WFS1 gene in HEK cells induces pathways related to neurodegeneration and mitochondrial damage. Physiol Genom 45:182–190. https://doi.org/10.1152/physiolgenomics.00122.2012
27. Kukley M, Capetillo-Zarate E, Dietrich D (2007) Vesicular glutamate release from axons in white matter. Nat Neurosci 10:311–320. https://doi.org/10.1038/nn1850
28. Kumar J, Ahmed A, Khan M, Ahmed Y (2023) There's more than meets the Eye: Wolfram Syndrome in a type I Diabetic Patient. J Med Cases 14:265–269. https://doi.org/10.14740/jmc4128
29. Kutz SM, Higgins CE, Higgins PJ (2012) Novel combinatorial therapeutic targeting of PAI-1 (SERPINE1) gene expression in Alzheimer's Disease. Mol Med Ther 1:106. https://doi.org/10.4172/2324-8769.1000106
30. Lebas H, Guérit S, Picot A, Boulay AC, Fournier A, Vivien D, Cohen Salmon M, Docagne F, Bardou I (2022) PAI-1 production by reactive astrocytes drives tissue dysfibrinolysis in multiple sclerosis models. Cell Mol Life Sci 79:323. https://doi.org/10.1007/s00018-022-04340-z
31. Lee TW, Tsang VWK, Birch NP (2015) Physiological and pathological roles of tissue plasminogen activator and its inhibitor neuroserpin in the nervous system. Front Cell Neurosci 9. https://doi.org/10.3389/fncel.2015.00396
32. Lee EM, Verma M, Palaniappan N, Pope EM, Lee S, Blacher L, Neerumalla P, An W, Campbell T, Brown Cet al et al (2023) Genotype and clinical characteristics of patients with Wolfram syndrome and WFS1-related disorders. Front Genet 14:1198171. https://doi.org/10.3389/fgene.2023.1198171

33. Lefevere E, Salinas-Navarro M, Andries L, Noterdaeme L, Etienne I, Van Wonterghem E, Vinckier S, Davis BM, Van Bergen T, Hove Iet al et al (2020) Tightening the retinal glia limitans attenuates neuroinflammation after optic nerve injury. Glia 68:2643–2660. https://doi.org/10.1002/glia.23875

34. Li H, Handsaker B, Wysoker A, Fennell T, Ruan J, Homer N, Marth G, Abecasis G, Durbin R (2009) The sequence Alignment/Map format and SAMtools. Bioinformatics 25:2078–2079. https://doi.org/10.1093/bioinformatics/btp352

35. Lin W, Popko B (2009) Endoplasmic reticulum stress in disorders of myelinating cells. Nat Neurosci 12:379–385. https://doi.org/10.1038/nn.2273

36. Lindsey JD, Scadeng M, Dubowitz DJ, Crowston JG, Weinreb RN (2007) Magnetic resonance imaging of the visual system in vivo: transsynaptic illumination of V1 and V2 visual cortex. NeuroImage 34:1619–1626. https://doi.org/10.1016/j.neuroimage.2006.07.048

37. Loncke J, Vervliet T, Parys JB, Kaasik A, Bultynck G (2021) Uniting the divergent Wolfram syndrome-linked proteins WFS1 and CISD2 as modulators of ca(2+) signaling. Sci Signal 14:eabc6165. https://doi.org/10.1126/scisignal.abc6165

38. Looser ZJ, Barrett MJP, Hirrlinger J, Weber B, Saab AS (2018) Intravitreal AAV-Delivery of genetically encoded sensors enabling simultaneous two-Photon Imaging and Electrophysiology of Optic nerve axons. Front Cell Neurosci 12:377. https://doi.org/10.3389/fncel.2018.00377

39. Looser ZJ, Faik Z, Ravotto L, Zanker HS, Jung RB, Werner HB, Ruhwedel T, Möbius W, Bergles DE Barros LF (2024) oligodendrocyte-axon metabolic coupling is mediated by extracellular K(+) and maintains axonal health. Nat Neurosci: Doi https://doi.org/10.1038/s41593-023-01558-3

40. López-Cano M, Fernández-Dueñas V, Ciruela F (2019) Proximity ligation assay image analysis protocol: addressing receptor-receptor interactions. Methods Mol Biol 2040:41–50. https://doi.org/10.1007/978-1-4939-9686-5_3

41. Love MI, Huber W, Anders S (2014) Moderated estimation of Fold change and dispersion for RNA-seq data with DESeq2. Genome Biol 15:550. https://doi.org/10.1186/s13059-014-0550-8

42. Lugar HM, Koller JM, Rutlin J, Marshall BA, Kanekura K, Urano F, Bischoff AN, Shimony JS, Hershey T, Washington University Wolfram Syndrome Research Study G (2016) Neuroimaging evidence of deficient axon myelination in Wolfram syndrome. Sci Rep 6:21167. https://doi.org/10.1038/srep21167

43. Lugar HM, Koller JM, Rutlin J, Eisenstein SA, Neyman O, Narayanan A, Chen L, Shimony JS, Hershey T (2019) Evidence for altered neurodevelopment and neurodegeneration in Wolfram syndrome using longitudinal morphometry. Sci Rep 9:6010. https://doi.org/10.1038/s41598-019-42447-9

44. Luuk H, Plaas M, Raud S, Innos J, Sütt S, Lasner H, Abramov U, Kurrikoff K, Kõks S, Vasar E (2009) Wfs1-deficient mice display impaired behavioural adaptation in stressful environment. Behav Brain Res 198:334–345. https://doi.org/10.1016/j.bbr.2008.11.007

45. Marshall BA, Permutt MA, Paciorkowski AR, Hoekel J, Karzon R, Wasson J, Viehover A, White NH, Shimony JS, Manwaring Let al et al (2013) Phenotypic characteristics of early Wolfram syndrome. Orphanet J Rare Dis 8:64. https://doi.org/10.1186/1750-1172-8-64

46. Miranda E, Galliciotti G (2022) Elucidating the pathological mechanisms of neurodegeneration in the lethal serpinopathy FENIB. Neural Regen Res 17:1733–1734. https://doi.org/10.4103/1673-5374.332142

47. Mishra R, Chen BS, Richa P, Yu-Wai-Man P (2021) Wolfram syndrome: new pathophysiological insights and therapeutic strategies. Ther Adv Rare Dis 2:26330040211039518. https://doi.org/10.1177/26330040211039518

48. Morikawa S, Urano F (2022) The role of ER stress in diabetes: exploring pathological mechanisms using Wolfram Syndrome. Int J Mol Sci 24. https://doi.org/10.3390/ijms24010230

49. Morikawa S, Blacher L, Onwumere C, Urano F (2022) Loss of function of WFS1 causes ER stress-mediated inflammation in pancreatic Beta-cells. Front Endocrinol 13:849204. https://doi.org/10.3389/fendo.2022.849204

50. Moura DMS, Brennan EJ, Brock R, Cocas LA (2021) Neuron to Oligodendrocyte Precursor Cell synapses: protagonists in Oligodendrocyte Development and Myelination, and targets for therapeutics. Front Neurosci 15:779125. https://doi.org/10.3389/fnins.2021.779125

51. Nami F, Ramezankhani R, Vandenabeele M, Vervliet T, Vogels K, Urano F, Verfaillie C (2021) Fast and efficient generation of Isogenic Induced Pluripotent Stem Cell Lines using Adenine Base editing. Crispr j 4:502–518. https://doi.org/10.1089/crispr.2021.0006

52. Nave KA, Asadollahi E, Sasmita A (2023) Expanding the function of oligodendrocytes to brain energy metabolism. Curr Opin Neurobiol 83:102782. https://doi.org/10.1016/j.conb.2023.102782

53. Neyrinck K, Van Den Daele J, Vervliet T, De Smedt J, Wierda K, Nijs M, Vanbokhoven T, D'hondt A, Planque M, Fendt S-M al (2021) SOX9-induced generation of functional astrocytes supporting neuronal maturation in an all-human system. Stem Cell Reviews Rep 17:1855–1873. https://doi.org/10.1007/s12015-021-10179-x

54. Panfili E, Mondanelli G, Orabona C, Belladonna ML, Gargaro M, Fallarino F, Orecchini E, Prontera P, Proietti E Frontino G (2021) novel mutations in the WFS1 gene are associated with Wolfram syndrome and systemic inflammation. Hum Mol Genet 30: 265–276 https://doi.org/10.1093/hmg/ddab040

55. Pang Z, Zhou G, Ewald J, Chang L, Hacariz O, Basu N, Xia J (2022) Using MetaboAnalyst 5.0 for LC–HRMS spectra processing, multi-omics integration and covariate adjustment of global metabolomics data. Nat Protoc 17:1735–1761. https://doi.org/10.1038/s41596-022-00710-w

56. Patergnani S, Bataillard MS, Danese A, Alves S, Cazevieille C, Valéro R, Tranebjærg L, Maurice T, Pinton P Delprat B The Wolfram-like variant WFS1E864K destabilizes MAM and compromises autophagy and mitophagy in human and mice. Autophagy: 1–12 https://doi.org/10.1080/15548627.2024.2341588

57. Perlmutter DH (2016) α1-antitrypsin Deficiency: a misfolded secretory protein variant with Unique effects on the endoplasmic reticulum. Endoplasmic Reticulum Stress Dis 3:63–72. https://doi.org/10.1515/ersc-2016-0004

58. Plaas M, Seppa K, Reimets R, Jagomäe T, Toots M, Koppel T, Vallisoo T, Nigul M, Heinla I, Meier R et al (2017) Wfs1- deficient rats develop primary symptoms of Wolfram syndrome: insulin-dependent diabetes, optic nerve atrophy and medullary degeneration. Scientific reports 7: 10220–10220 https://doi.org/10.1038/s41598-017-09392-x

59. Pourtoy-Brasselet S, Sciauvaud A, Boza-Moran MG, Cailleret M, Jarrige M, Polvèche H, Polentes J, Chevet E, Martinat C, Peschanski M al (2021) Human iPSC-derived neurons reveal early developmental alteration of neurite outgrowth in the late-occurring neurodegenerative Wolfram syndrome. Am J Hum Genet 108:2171–2185. https://doi.org/10.1016/j.ajhg.2021.10.001

60. proteinatlas.org (2024) The Human Protein Atlas https://www.proteinatlas.org/ENSG00000109501-WFS1. Accessed 11 Jul 2024

61. Prusky GT, Alam NM, Beekman S, Douglas RM (2004) Rapid quantification of adult and developing mouse spatial vision using a virtual optomotor system. Invest Ophthalmol Vis Sci 45:4611–4616

62. Raud S, Sutt S, Luuk H, Plaas M, Innos J, Koks S, Vasar E (2009) Relation between increased anxiety and reduced expression of alpha1 and alpha2 subunits of GABA(A) receptors in Wfs1-deficient mice. Neurosci Lett 460:138–142. https://doi.org/10.1016/j.neulet.2009.05.054

63. Reuland CJ, Church FC (2020) Synergy between plasminogen activator inhibitor-1, α-synuclein, and neuroinflammation in Parkinson's disease. Med Hypotheses 138:109602. https://doi.org/10.1016/j.mehy.2020.109602

64. Rigoli L, Bramanti P, Di Bella C, De Luca F (2018) Genetic and clinical aspects of Wolfram syndrome 1, a severe neurodegenerative disease. Pediatr Res 83:921–929. https://doi.org/10.1038/pr.2018.17

65. Rojas-Rivera D, Armisén R, Colombo A, Martínez G, Eguiguren AL, Díaz A, Kiviluoto S, Rodríguez D, Patron M, Rizzuto R et al (2012) TMBIM3/GRINA is a novel unfolded protein response (UPR) target gene that controls apoptosis through the modulation of ER calcium homeostasis. Cell Death & Differentiation 19: 1013–1026 https://doi.org/10.1038/cdd.2011.189

66. Rossi G, Ordazzo G, Vanni NN, Castoldi V, Iannielli A, Di Silvestre D, Bellini E, Bernardo L, Giannelli SG, Luoni Met al et al (2023) MCT1-dependent energetic failure and neuroinflammation underlie optic nerve degeneration in Wolfram syndrome mice. eLife 12. https://doi.org/10.7554/eLife.81779

67. Saab AS, Nave KA (2017) Myelin dynamics: protecting and shaping neuronal functions. Curr Opin Neurobiol 47:104–112. https://doi.org/10.1016/j.conb.2017.09.013

68. Samara A, Rahn R, Neyman O, Park KY, Samara A, Marshall B, Dougherty J, Hershey T (2019) Developmental hypomyelination in Wolfram syndrome: new insights from neuroimaging and gene expression analyses. Orphanet J Rare Dis 14:279. https://doi.org/10.1186/s13023-019-1260-9

69. Samara A, Lugar HM, Hershey T, Shimony JS (2020) Longitudinal Assessment of Neuroradiologic Features in Wolfram Syndrome. AJNR Am J Neuroradiol 41:2364–2369. https://doi.org/10.3174/ajnr.A6831

70. Schmidt-Kastner R, Kreczmanski P, Preising M, Diederen R, Schmitz C, Reis D, Blanks J, Dorey CK (2009) Expression of the diabetes risk gene wolframin (WFS1) in the human retina. Exp Eye Res 89:568–574. https://doi.org/10.1016/j.exer.2009.05.007

71. Sepúlveda MR, Dresselaers T, Vangheluwe P, Everaerts W, Himmelreich U, Mata AM, Wuytack F (2012) Evaluation of manganese uptake and toxicity in mouse brain during continuous MnCl2 administration using osmotic pumps. Contrast Media Mol Imaging 7:426–434. https://doi.org/10.1002/cmmi.1469

72. Sergeys J, Etienne I, Van Hove I, Lefevere E, Stalmans I, Feyen JHM, Moons L, Van Bergen T (2019) Longitudinal in vivo characterization of the

Streptozotocin-Induced Diabetic Mouse Model: focus on early inner retinal responses. Invest Ophthalmol Vis Sci 60:807–822. https://doi.org/10.1167/iovs.18-25372

73. Szklarczyk D, Kirsch R, Koutrouli M, Nastou K, Mehryary F, Hachilif R, Gable AL, Fang T, Doncheva NT, Pyysalo Set al et al (2023) The STRING database in 2023: protein-protein association networks and functional enrichment analyses for any sequenced genome of interest. Nucleic Acids Res 51:D638–d646. https://doi.org/10.1093/nar/gkac1000

74. Takeda K, Inoue H, Tanizawa Y, Matsuzaki Y, Oba J, Watanabe Y, Shinoda K, Oka Y (2001) WFS1 (Wolfram syndrome 1) gene product: predominant subcellular localization to endoplasmic reticulum in cultured cells and neuronal expression in rat brain. Hum Mol Genet 10:477–484. https://doi.org/10.1093/hmg/10.5.477

75. Takei D, Ishihara H, Yamaguchi S, Yamada T, Tamura A, Katagiri H, Maruyama Y, Oka Y (2006) WFS1 protein modulates the free ca(2+) concentration in the endoplasmic reticulum. FEBS Lett 580:5635–5640. https://doi.org/10.1016/j.febslet.2006.09.007

76. Thornton MA, Hughes EG (2020) Neuron-oligodendroglia interactions: activity-dependent regulation of cellular signaling. Neurosci Lett 727:134916. https://doi.org/10.1016/j.neulet.2020.134916

77. Urano F (2016) Wolfram Syndrome: Diagnosis, Management, and Treatment. Curr Diab Rep 16: 6 https://doi.org/10.1007/s11892-015-0702-6

78. Vandenabeele M, Veys L, Lemmens S, Hadoux X, Gelders G, Masin L, Serneels L, Theunis J, Saito T, Saido TC al (2021) The App(NL-G-F) mouse retina is a site for preclinical Alzheimer's disease diagnosis and research. Acta Neuropathol Commun 9(6). https://doi.org/10.1186/s40478-020-01102-5

79. Visnapuu T, Plaas M, Reimets R, Raud S, Terasmaa A, Koks S, Sutt S, Luuk H, Hundahl CA, Eskla KL al (2013) Evidence for impaired function of dopaminergic system in Wfs1-deficient mice. Behav Brain Res 244:90–99. https://doi.org/10.1016/j.bbr.2013.01.046

80. Yu G, Wang LG, Han Y, He QY (2012) clusterProfiler: an R package for comparing biological themes among gene clusters. Omics 16:284–287. https://doi.org/10.1089/omi.2011.0118

81. Yuan F, Li Y, Hu R, Gong M, Chai M, Ma X, Cha J, Guo P, Yang K, Li M al (2023) Modeling disrupted synapse formation in Wolfram syndrome using hESCs-derived neural cells and cerebral organoids identifies Riluzole as a therapeutic molecule. Mol Psychiatry 28:1557–1570. https://doi.org/10.1038/s41380-023-01987-3

82. Zatyka M, Da Silva Xavier G, Bellomo EA, Leadbeater W, Astuti D, Smith J, Michelangeli F, Rutter GA, Barrett TG (2014) Sarco(endo)plasmic reticulum ATPase is a molecular partner of Wolfram syndrome 1 protein, which negatively regulates its expression. Hum Mol Genet 24:814–827. https://doi.org/10.1093/hmg/ddu499

83. Zatyka M, Rosenstock TR, Sun C, Palhegyi AM, Hughes GW, Lara-Reyna S, Astuti D, di Maio A, Sciauvaud A, Korsgen ME al (2023) Depletion of WFS1 compromises mitochondrial function in hiPSC-derived neuronal models of Wolfram syndrome. Stem cell Rep 18:1090–1106. https://doi.org/10.1016/j.stemcr.2023.04.002

84. Zatyka M, Rosenstock TR, Sun C, Palhegyi AM, Hughes GW, Lara-Reyna S, Astuti D, di Maio A, Sciauvaud A, Korsgen ME al (2023) Depletion of WFS1 compromises mitochondrial function in hiPSC-derived neuronal models of Wolfram syndrome. Stem cell Rep 18:1090–1106. https://doi.org/10.1016/j.stemcr.2023.04.002

85. Zhu Y, Burg T, Neyrinck K, Vervliet T, Nami F, Vervoort E, Ahuja K, Sassano ML, Chai YC, Tharkeshwar AKet al et al (2024) Disruption of MAM integrity in mutant FUS oligodendroglial progenitors from hiPSCs. Acta Neuropathol 147:6. https://doi.org/10.1007/s00401-023-02666-x

86. Ziskin JL, Nishiyama A, Rubio M, Fukaya M, Bergles DE (2007) Vesicular release of glutamate from unmyelinated axons in white matter. Nat Neurosci 10:321–330. https://doi.org/10.1038/nn1854

87. Zonouzi M, Scafidi J, Li P, McEllin B, Edwards J, Dupree JL, Harvey L, Sun D, Hübner CA Cull-candy SG (2015) GABAergic regulation of cerebellar NG2 cell development is altered in perinatal white matter injury. Nat Neurosci 18:674–682 https://doi.org/10.1038/nn.3990

Publisher's Note

Springer Nature remains neutral with regard to jurisdictional claims in published maps and institutional affiliations.